

Asymmetric Responses of the Western Tropical Pacific Sea Level to El Niño and La Niña

WANG Fan¹, Ren Qiuping², Li Yuanlong³, Zheng Fei⁴, and Duan Jing⁵

¹Institute of Oceanology, Chinese Academy of Sciences Qingdao, China

²Key Laboratory of Ocean Circulation and Waves, Institute of Oceanology, Chinese Academy of Sciences

³Institute of Oceanology, Chinese Academy of Sciences

⁴Institute of Atmospheric Physics

⁵Institute of Oceanology, Chinese Academy of Sciences

November 16, 2022

Abstract

The western tropical Pacific (WTP) exhibits large interannual sea level anomalies (SLAs), and the sea level falling in El Niño is evidently stronger than the rising in La Niña. The asymmetry is most prominent near 160°E with the response to El Niño larger by three times and becomes less obvious near the western boundary. Sensitivity experiments of a simplified ocean model suggest that the asymmetry in surface wind forcing structure between El Niño and La Niña is critical. The El Niño's westerly wind anomaly patch locates more east than the La Niña's easterly wind patch during the mature stage, and its upwelling effects are accumulated over a wider longitude range and cause stronger negative SLAs in the WTP. Near the western boundary, however, upwelling effects are attenuated by easterly wind anomalies during El Niño conditions. The asymmetric ocean responses to ENSO winds may participate in the asymmetry of ENSO cycle.

1 Submitted to *Geophysical Research Letters*

2 Asymmetric Responses of the Western Tropical Pacific Sea Level to
3 El Niño and La Niña

4 Qiuping Ren^{1,2}, Yuanlong Li^{1,3,4}, Fei Zheng^{3,5}, Fan Wang^{1,2,3,4,*},
5 Jing Duan^{1,3,4}

6

7 ¹Key Laboratory of Ocean Circulation and Waves, Institute of Oceanology, Chinese Academy of
8 Sciences, Qingdao, China,

9 ²University of Chinese Academy of Sciences, Beijing, China,

10 ³Center for Ocean Mega-Science, Chinese Academy of Sciences, Qingdao, China,

11 ⁴Function Laboratory for Ocean Dynamics and Climate, Qingdao National Laboratory for Marine
12 Science and Technology, Qingdao, China,

13 ⁵International Center for Climate and Environment Science, Institute of Atmospheric Physics, Chinese
14 Academy of Sciences, Beijing, China,

15

April 2020

*Corresponding Author:

Fan Wang

Key Laboratory of Ocean Circulation and Waves, Institute of Oceanology, Chinese
Academy of Sciences, Qingdao 266071, China.

Email: fwang@qdio.ac.cn

16 **Key Points.**

- 17 1) The responses of the western tropical Pacific sea level to ENSO are
18 obviously asymmetric, and the response to El Niño is evidently stronger.
- 19 2) The different surface wind anomaly structure between El Niño and La Niña
20 is critical for the asymmetric response of sea level.
- 21 3) The asymmetric ocean responses to ENSO may contribute to the ENSO
22 asymmetry.

23 **Abstract**

24 The western tropical Pacific (WTP) exhibits large interannual sea level
25 anomalies (SLAs), and the sea level falling in El Niño is evidently stronger than the
26 rising in La Niña. The asymmetry is most prominent near 160°E with the response to
27 El Niño larger by three times and becomes less obvious near the western boundary.
28 Sensitivity experiments of a simplified ocean model suggest that the asymmetry in
29 surface wind forcing structure between El Niño and La Niña is critical. The El Niño's
30 westerly wind anomaly patch locates more east than the La Niña's easterly wind patch
31 during the mature stage, and its upwelling effects are accumulated over a wider
32 longitude range and cause stronger negative SLAs in the WTP. Near the western
33 boundary, however, upwelling effects are attenuated by easterly wind anomalies
34 during El Niño conditions. The asymmetric ocean responses to ENSO winds may
35 participate in the asymmetry of ENSO cycle.

36 **Plain Language Summary**

37 ENSO is the most influential climate variability mode of the Pacific and causes
38 strong interannual sea level anomalies (SLAs) in the western tropical Pacific (WTP).
39 We notice that the WTP's sea level falling in El Niño condition is stronger than its sea
40 level rising in La Niña. This difference is most prominent near 160°E, where the
41 falling in El Niño is stronger by three times. This phenomenon becomes much less
42 evident near the western boundary of the Pacific basin. We find that the difference in
43 surface wind anomaly structures between El Niño and La Niña is the primary cause.
44 El Niño's westerly wind anomaly center locates more east than La Niña's easterly

45 wind anomaly center in their mature phase, and there are easterly wind anomalies
46 emerging near the western boundary during El Niño. Therefore, effect of El Niño's
47 westerly wind anomaly is accumulated over a wider longitude range and causes
48 stronger sea level falling in the WTP. But this effect becomes weaker near the western
49 boundary, due to easterly wind anomalies there. By contrast, effect of La Niña's
50 easterly wind anomaly strengthens monotonically from east to west, but the produced
51 sea level rising signatures are mainly confined to the WTP.

52 **Keywords**

53 Western Tropical Pacific, Sea Level, ENSO, ENSO asymmetry, Interannual

54 Variability

55 **1. Introduction**

56 Regional sea level change, as an essential aspect of climate change, is attracting
57 increasing attention of scientific communities and the general public, because of its
58 threats on eco-systems and people of coastal residence (e.g., Nicholls & Cazenave,
59 2010; Cazenave & Cozannet, 2014). There is a paramount demand for improved
60 understanding of regional sea level changes on various timescales (e.g., Milne et al.,
61 2009; Church et al., 2013; Stammer et al., 2013). Sea level changes over the tropical
62 Pacific Ocean are particularly pronounced on interannual timescale, as largely
63 modulated by El Niño-Southern Oscillation (ENSO) (e.g., Cazenave et al., 2008;
64 Antonov et al., 2005; Cheng et al., 2008). It is evident in Figure 1a that the western
65 tropical Pacific (WTP) shows stronger interannual sea level anomalies (SLAs) than
66 other regions, as quantified the standard deviation of low-passed SLAs. The WTP
67 shows strong sea level rising (falling) during the La Niña (El Niño) condition, as a
68 result of prevailing easterly (westerly) wind anomalies over the tropical Pacific basin
69 (Wyrтки, 1975; Zebiak, 1984; Alory & Delcroix, 2002; Gu & Li, 2009; Nerem et al.,
70 2010; Merrifield, 2011; Zhang & Church, 2012; Chang et al., 2013; Becker et al.,
71 2016; Hamlington et al., 2016; Wang, 2018). The sea level rising during La Niña
72 conditions is expected to aggravate coastal erosion, extreme marine flooding, or
73 saltwater intrusion in coastal aquifers (Nicholls & Tol, 2006; Nicholls et al., 2007;
74 Nicholls & Cazenave, 2010), thus becomes a major threat for the densely populated
75 coastal regions. However, the sea level falling during El Niño causes the coral reef
76 exposure and could damage the region's ecosystem. There are many

77 heavily-populated coasts and islands in the WTP, so the sea level changes during
78 ENSO are well worth studying.

79 El Niño and La Niña are, however, not mirrors of each other. They exhibit
80 obvious asymmetry in magnitude, duration time, and occurrence frequency (e.g., Yu
81 et al., 1997; Burgers & Stephenson, 1999; Ohba & Ueda, 2007; Gergis & Fowler,
82 2009; An & Choi, 2009; Okumura & Deser, 2010). Their signatures on sea level are
83 also asymmetric, owing to not only ENSO's asymmetry but also the nonlinearity in
84 ocean response (Niedzielski & Kosek, 2010; Swierczynska et al., 2013; Im et al.,
85 2015; An & Kim, 2017). Previous studies have demonstrated that ENSO asymmetry is
86 contributed by nonlinear dynamical heating of ocean current advection (e.g., Kang &
87 Kug, 2002; Jin et al., 2003; An & Jin, 2004; Su et al., 2010). As dynamically
88 associated with the upper-ocean currents through pressure gradient, the asymmetric
89 SLAs induced by ENSO may affect ocean current advection of heat and thereby
90 participate in the ENSO asymmetry.

91 In this study, we aim to investigate the asymmetric response of the WTP sea
92 level to ENSO and the underlying dynamical processes. This effort is of paramount
93 need for the prediction and projection of regional sea level change and adaptations of
94 the low-lying coasts and islands, as well as for understanding the dynamics of ENSO
95 asymmetry. The rest of the paper is structured as follows. Section 2 describes the data
96 and models. Section 3 describes the asymmetric SLAs of the WTP in response to
97 ENSO. Section 4 explores the underlying dynamics through a simplified ocean model.
98 Section 5 presents concluding remarks.

99 **2. Data and Models**

100 **2.1. Data**

101 In this study we use $0.25^\circ \times 0.25^\circ$, monthly satellite SLA data of 1993-2016
102 from Archiving Validation, and Interpretation of Satellite Oceanography (AVISO; Le
103 Traon et al., 1998) and sea level records of three tidal gauge stations in the WTP:
104 Malakal at 7.33°N , 134.45°E for 1979-2016, Kapingamrangi at 1.1°N , 154.78°E for
105 1929-2016, and Lombrum at 2.04°S , 147.47°E for 1995-2016 (Figure S1 in the
106 Supporting Information). The Hadley Centre Sea Ice and Sea Surface Temperature
107 (HadISST) data set (Kennedy et al., 2011) of the Met Office during 1979-2016 with
108 horizontal resolution of $1^\circ \times 1^\circ$ is used to compute Niño-3.4 index and identify El
109 Niño and La Niña conditions. Surface winds and other surface atmospheric fields of
110 1979-2016 are taken from the 0.75° monthly dataset of the European Centre for
111 Medium-Range Weather Forecasts (ECMWF) ERA-interim (Dee et al., 2011).

112 **2.2. HYCOM**

113 The HYbrid Coordinate Ocean Model (HYCOM) version 2.2.18 (Bleck, 2002)
114 are used to simulate interannual SLAs in the tropical Pacific Ocean. HYCOM is
115 configured to the Pacific Ocean basin between 48°S - 48°N , 110°E - 70°W , with a
116 horizontal resolution of $1/3^\circ \times 1/3^\circ$ and 26 hybrid vertical layers (Li et al., 2015; Ren et
117 al., 2020). Surface atmospheric forcing fields (winds, heat fluxes, precipitation, etc.)
118 are taken from ERA-interim. Three sponge layers are applied to the western, southern
119 and northern open-ocean boundaries, where model temperature and salinity are
120 related to the World Ocean Atlas 2009 (WOA09) climatology (Antonov et al., 2010).

121 More details of model configuration are described in Ren et al. (2020). Subsequent to
122 the spin-up run of 30 years under monthly climatologic forcing, two parallel
123 experiments are performed under daily ERA-Interim fields for the period of
124 1979-2016. The control run (HYCOM-CTL) is forced with the original daily
125 atmospheric fields and assumed to contain the complete processes. This experiment
126 can well reproduce the amplitude and spatial distribution of interannual SLA and
127 upper-ocean circulation variation in observation (Figure 1b; Ren et al., 2020). Another
128 experiment, HYCOM-TAU, uses daily wind stress forcing as HYCOM-CTL, but all
129 the other forcing fields (heat and freshwater fluxes) are fixed to monthly climatology.
130 HYCOM-TAU is used to evaluate the effects of wind forcing on sea level.

131 **2.3. Reduced-Gravity Ocean Model**

132 To achieve more in-depth understanding, a series of experiments are performed
133 with a 1.5-layer nonlinear reduced-gravity ocean (RGO) model. This model mainly
134 represents the 1st-mode baroclinic response of the ocean to surface wind forcing,
135 which is the dominant source of large-scale interannual variability in sea level and
136 upper-ocean circulation of the WTP (e.g., Qiu & Chen, 2010, 2012). The model is
137 configured to the Pacific Ocean basin between 40°S-40°N, 100°E-70°W with
138 horizontal resolutions of 0.25°×0.25° and forced by monthly ERA-Interim surface
139 winds. Readers are referred to Duan et al. (2019) for more details of the model
140 configuration. After a spin-up of 10 years under climatological wind forcing, the
141 control run of RGO model (RGO-CTL) is forced by realistic monthly winds. RGO
142 model experiments (Table S1) are forced by idealized wind forcing to examine the

143 role of wind forcing asymmetry and are described in Section 4.

144 **3. Asymmetric Responses to El Niño and La Niña**

145 To highlight the interannual variations associated with ENSO, we analyze the
146 13-month low-pass filtered anomaly fields with the monthly climatology removed.
147 Skewness S is a measure of the distribution asymmetry with $S = 0$ indicating a normal
148 distribution (White, 1980). Figure 1c shows the skewness of the observed SLA over
149 the tropical Pacific for 1993-2016. The eastern tropical Pacific is positively skewed
150 with the maximum S of ~ 2.0 , while the central-western tropical Pacific is negatively
151 skewed with the minimum S of -2.0 and a horseshoe structure extending from the
152 equator to extratropical regions in both hemispheres. This distribution of SLA
153 skewness resembles that of SST anomaly (An & Jin, 2004; Niedzielski & Kosek,
154 2010) and is likely associated with the positive skewness of ENSO (Nerem et al.,
155 2010). The El Niño condition is characterized by positive SLAs in the eastern Pacific
156 and negative SLAs in the WTP, and these anomalies are stronger in amplitude than
157 the opposite SLAs occurring in La Niña condition (Niedzielski & Kosek, 2010;
158 Figure S1).

159 In addition to the asymmetry residing in ENSO (e.g., as quantified by the
160 skewness of Niño-3.4 index), the asymmetric responses of sea level to El Niño and La
161 Niña also contribute to the SLA asymmetry shown in Figure 1c. We regress SLAs
162 onto the normalized Niño-3.4 index separately for the El Niño condition (Niño-3.4 >
163 0) and the La Niña condition (Niño-3.4 < 0). The corresponding regression
164 coefficients, namely $k_{\text{Niño}}$ and $k_{\text{Niña}}$, are used to quantify the responses of SLA to El

165 Niño and La Niña, respectively (Figures 1d and 1e). The response time of sea level to
166 ENSO shows spatial variation, as indicated by the lead-lag correlation (Figure S2a).
167 For each grid point, the lead-lag time of the maximal correlation is used to compute
168 the regression coefficient. The results are not dramatically different from those of
169 simultaneous regression (Figure S2b). Figures 1d and 1e show distributions of $k_{\text{Niño}}$
170 and $k_{\text{Niña}}$. In the WTP, the maximal $k_{\text{Niño}}$ of ~ -0.2 m is located 20° - 30° away from the
171 western boundary, and $k_{\text{Niño}}$ decreases in magnitude as approaching the western
172 boundary. By contrast, the peak $k_{\text{Niña}}$ values of ~ -0.15 m are close to the western
173 boundary. We further use the ratio of $k_{\text{Niño}}$ to $k_{\text{Niña}}$ to quantify the response asymmetry,

$$174 \quad R_k = \frac{k_{\text{Niño}}}{k_{\text{Niña}}}. \quad (1)$$

175 $R_k = 1$ denotes symmetric response of SLAs to El Niño and La Niña, while $R_k > 1$ and
176 $R_k < 1$ indicates stronger and weaker response to El Niño than to La Niña, respectively.
177 As shown in Figure 1f, R_k reaches the largest value near 160°E with values exceeding
178 3.0, indicating that the response of SLA to El Niño is stronger by at least 3 times than
179 the response to La Niña. R_k is weakened to ~ 1.0 near the western boundary, implying
180 SLA responses there are nearly symmetric. This interesting distribution of R_k in the
181 WTP and underlying dynamics are worthy of systematic investigation. One may
182 notice that R_k is < 1 in the central Pacific and is > 1 in the eastern Pacific, indicative
183 of prevailing asymmetry over the tropical Pacific basin. In the following, we focus on
184 explaining the R_k distribution in the WTP.

185 Simulations of HYCOM and RGO model have faithfully reproduced the
186 observed interannual variations of sea level at three tidal gauge stations (Figure S3).

187 The upper-layer thickness (ULT) anomaly of the 1.5-layer RGO model is a good
188 proxy of SLA in the tropical Pacific (e.g., Qiu & Chen, 2010, 2012; Chang et al., 2013;
189 Duan et al., 2019). The correlations among AVISO, HYCOM-CTL, HYCOM-TAU
190 and RGO-CTL at the three tidal gauge stations are all above 0.85. The asymmetric
191 responses of SLAs to El Niño and La Niña in the WTP during 1993-2016 can be
192 realistically reproduced by HYCOM-CTL, HYCOM-TAU, and RGO-CTL (Figures
193 2a-2c), although RGO-CTL fails to capture the features in the eastern Pacific. The
194 good performance of HYCOM-TAU and RGO-CTL indicates that the interannual
195 SLAs in the WTP and their asymmetric features are primarily the results of ENSO
196 wind forcing, and the underlying dynamics can be explored by sensitive model
197 experiments with prescribed wind forcing fields.

198 **4. Dynamics**

199 To include more ENSO events, we use the period of 1979-2016 to perform
200 model experiments (Table S1), although R_k of 1979-2016 shows detailed differences
201 from that of 1993-2016 in the northwest Pacific (Figures 2d-2f). According to existing
202 studies of ENSO asymmetry, the different spatial and temporal characteristics of wind
203 anomalies are essential to cause the SST asymmetry between El Niño and La Niña
204 (Kang & Kug, 2002; An & Kim, 2017). To examine which aspect of ENSO's wind
205 forcing is critical in regulating the asymmetric responses of SLAs, we adopt a
206 statistical model based on the singular value decomposition (SVD) of wind stress and
207 SST (Kang & Kug, 2000), which is expressed as

$$208 \quad \mathbf{\tau}'(x, y, t) = \sum_n^N c(n) [\sum_{x,y} V_{\text{SST}}(x, y, n) T(x, y, t)] V_{\tau}(x, y, n), \quad (2)$$

209 where x , y , and t represent longitude, latitude, and time, respectively, V_{SST} and V_{τ} are
 210 the SVD singular vectors for SST and wind stress, T is the SST anomaly field, and n
 211 $= 1, 2, \dots, N$ indicates the n th mode of SVD, $\sum_{x,y}$ indicates spatial integration over
 212 the region of 100°-290°E, 40°S-40°N. $c(n)$ represents the correlation between SST
 213 and wind stress anomalies,

$$214 \quad c(n) = \frac{\sum_t t_{\text{SST}}(t,n)t_{\tau}(t,n)}{\sum_t t_{\text{SST}}(t,n)^2}, \quad (3)$$

215 where t_{SST} and t_{τ} are the corresponding time series, the numerator is the covariance
 216 of t_{SST} and t_{τ} and the denominator is the variance of t_{SST} , and \sum_t indicates temporal
 217 integration from January 1979 to December 2016. Zonal and meridional components
 218 of τ' are separately computed. All the RGO sensitive experiments are forced by
 219 monthly wind stress anomalies constructed by Eq. 2 (representing ENSO wind
 220 forcing) plus monthly climatological winds.

221 We first perform two experiments, namely EXP1 and EXP2. EXP1 uses different
 222 wind stress anomaly fields for El Niño and La Niña conditions. Specifically, $\tau'_{\text{Niño}}$ and
 223 $\tau'_{\text{Niña}}$ are reconstructed separated for Niño-3.4 ≥ 0 and Niño-3.4 < 0 conditions
 224 (Figures S4a and S4b) using Eq. 2, respectively, so that the synthesized τ' still retains
 225 the difference in spatial structure between El Niño and La Niña conditions. By
 226 contrast, EXP2 does not distinguish El Niño and La Niña conditions and uses
 227 reconstructed τ' for the entire model period (Figure S4c). As such, the difference
 228 between EXP1 and EXP2 represents the effect of different wind anomaly structures
 229 between El Niño and La Niña on SLAs. In EXP1 and EXP2, we use only the leading
 230 mode ($n = 1$) of SVD to reconstruct τ' (Figure S4), which explains $> 85\%$ of the total

231 covariance and mainly represents ENSO's mature phase (Figure S5). The higher SVD
232 modes largely represent the transition stages between El Niño and La Niña polarities
233 (Figure S5) and have limited impacts on the asymmetry of SLAs (Figure S6).

234 Figures 3a and 3b show R_k distributions of ULT produced by EXP1 and EXP2,
235 respectively. EXP1 is able to reproduce large R_k values in the WTP as RGO-CTL,
236 whereas R_k is generally close to 1.0 in EXP2. These results suggest that the
237 asymmetry in surface wind structures between El Niño and La Niña is largely
238 responsible for asymmetric responses of the WTP sea level. Note that EXP2 still
239 retains some asymmetric characteristics of ENSO winds, such as the asymmetries in
240 intensity, frequency, and temporal evolution. Figure 3b however indicates that these
241 factors have little contributions to SLA asymmetry. This is confirmed by an additional
242 experiment EXP3, which adopts an idealized sine time series for τ' (Table S1) and
243 achieves similar results to EXP2 (Figure S7).

244 In the equatorial zone, zonal component of wind stress τ^x is much more
245 influential for the ocean than the meridional component. We repeat EXP1 and EXP2
246 using only τ^x anomaly, and τ^y is fixed to monthly climatology (EXP1-TAUX and
247 EXP2-TAUX). The results of two experiments achieve are broadly consistent with
248 EXP1 and EXP2 (Figures 3c and 3d). Therefore, the spatial structure of τ^x is critical
249 for the asymmetric responses. The typical structures of ULT and τ^x in EXP1-TAUX
250 for warm and cold phases are shown in Figures 3e and 3f, respectively, as represented
251 by the leading SVD mode of τ^x and ULT. Notice that westerly wind anomaly patch of
252 El Niño locates more east than the easterly wind anomaly patch of La Niña in their

253 mature phase, and correspondingly the zero value of ULT anomaly of El Niño also
 254 locates more east (Jin, 1997; Kang & Kug, 2002). During El Niño there are easterly
 255 wind anomalies near the western boundary. The strong negative ULT anomalies in El
 256 Niño are seen over a wide longitude range and weaken as approaching the western
 257 boundary, while the positive ULT anomalies in La Niña are confined to the far WTP
 258 and generally strengthen westward.

259 To better elucidate how the wind forcing structure cause asymmetric SLAs, we
 260 show in Figure 4 the zonal distributions of τ^x and ULT in the equatorial band
 261 (5°S - 5°N). It is clearly discernible in Figure 4a that the El Niño’s westerly wind
 262 anomaly patch locates more east than the La Niña’s easterly wind anomaly patch. The
 263 forcing effect of equatorial zonal wind stress on sea level and ULT slopes can be
 264 roughly expressed in a linear relationship (Sverdrup, 1947; McCreary, 1977; Alory &
 265 Delcroix, 2002; Palanisamy et al., 2014),

$$266 \quad \frac{dh}{dx} = \tau^x, \quad (4)$$

267 where h is ULT anomaly or SLA. Therefore, $h(x)$ at a given longitude x can be
 268 determined by the integration of Eq. (4) from the eastern boundary $x_E = 70^\circ\text{W}$ along
 269 equator,

$$270 \quad h(x) = h(x_E) + \int_{x_E}^x \tau^x dx. \quad (5)$$

271 Since $h(x_E)$ diffuses quickly away from the eastern boundary as free Rossby waves
 272 and has little impact on the interior Pacific (Qiu et al., 2013), $h(x)$ is primarily
 273 determined by the zonal integral of τ^x from x_E to x (second term). As such, the
 274 negative ULT anomaly in El Niño in the WTP is much stronger than the positive ULT

275 anomaly in La Niña owing to the much wider westerly wind anomaly patch to its east.
 276 West of 160°E, easterly wind anomaly near the western boundary causes downwelling
 277 of the ocean, resulting in the attenuation of negative ULT anomalies there. By contrast,
 278 the La Niña's positive ULT anomalies are continuously strengthened by easterly wind
 279 anomalies. As a result, the ULT anomalies of El Niño and La Niña are comparable in
 280 amplitude in the far WTP, and the asymmetry of response is no longer evident there
 281 (right panel of Figure 4a). In EXP2-TAUX (Figure 4b), without the difference in wind
 282 forcing structure (left panel), the asymmetric responses cannot be reproduced (middle
 283 and right panels).

284 Figure 4c shows the zonal distributions of ULT anomaly and regression
 285 coefficients predicted by the linear theory, which compare favorably with Figure 4a. It
 286 indicates that the linear theory can to a large extent capture the processes causing
 287 asymmetric responses to ENSO winds and confirms the critical role played by the
 288 structure of zonal wind anomaly. Under this theoretical framework, the response
 289 asymmetry R_k can be theoretically expressed as,

$$290 \quad R_k(x) \approx \frac{\int_{x_E}^x \tau^x_{Nino} dx}{\int_{x_E}^x \tau^x_{Nina} dx}, \quad (6)$$

291 where τ^x_{Nino} and τ^x_{Nina} are the zonal wind stress anomaly in El Niño and La Niña
 292 conditions, respectively. Eq. (6) clearly suggests the sensitivity of $R_k(x)$ to the
 293 distribution of τ^x from x to the eastern boundary.

294 **5. Concluding Remarks**

295 The WTP exhibits large interannual variations of sea level, and the sea level

296 falling in El Niño is stronger than the rising in La Niña. Here we show that this
297 asymmetry is most prominent near 160°E with the response to El Niño larger by ~3
298 times and becomes much less obvious near the western boundary. RGO model
299 experiments suggest that the asymmetric surface wind anomaly structure between El
300 Niño and La Niña conditions is critical. El Niño's westerly wind anomaly patch
301 locates more east than La Niña's easterly wind anomaly patch in their mature stages.
302 As such, the upwelling effects of westerly wind anomalies are accumulated over a
303 wider longitude range and cause stronger negative SLAs in the WTP. As approaching
304 further toward the western boundary, positive SLAs in La Niña continue to amplify,
305 while negative SLAs of El Niño are attenuated by easterly wind anomalies in the far
306 WTP.

307 Here we reveal the sensitivity of the asymmetric SLAs in the WTP to the ENSO
308 wind structures. It is interesting to investigate whether the asymmetric SLAs in turn
309 contributes to the ENSO asymmetry in amplitude and temporal evolutions. This can
310 be investigated through careful heat budget analysis that evaluate the effects of
311 asymmetric current advection on SST variability. In addition, the zonal surface wind
312 patch dominates the SLA asymmetry along the equator, and its off-equatorial structure
313 may affect the asymmetry beyond the equator by modifying the wind stress curl (An
314 & Bong, 2016). In addition to wind forcing, the effects of local nonlinear processes,
315 such as mesoscale eddies, on sea level in the WTP are not resolved by the RGO
316 model experiments (Chen et al., 2015; Qiu et al., 2015), which can be also examined
317 in the future study.

318 **Acknowledgments**

319 This research is supported by National Natural Science Foundation of China
320 (grants 41730534 and 41806014) and the National Program on Global Change and
321 Air-Sea Interaction (grant GASI-IPOVAI-01-01). AVISO sea level data are available
322 at <http://marine.copernicus.eu/services-portfolio/access-to-products/>. Tidal gauges data
323 are available at <https://www.psmsl.org/>. ERA-Interim wind data are available at
324 <https://apps.ecmwf.int/datasets/>. HadISST data are downloaded from Met-Office
325 website <https://www.metoffice.gov.uk/hadobs/>.
326

327 **References**

- 328 Alory, G., and T. Delcroix (2002), Interannual sea level changes and associated mass
329 transports in the tropical Pacific from TOPEX/Poseidon data and linear model
330 results (1964-1999), *Journal of Geophysical Research-Oceans*, 107(C10), doi:
331 10.1029/2001jc001067.
- 332 An, S. I., and F. F. Jin (2004), Nonlinearity and asymmetry of ENSO, *Journal of*
333 *Climate*, 17(12), 2399-2412, doi:
334 10.1175/1520-0442(2004)017<2399:naaoe>2.0.co;2.
- 335 An, S.-I., and J. Choi (2009), Seasonal locking of the ENSO asymmetry and its
336 influence on the seasonal cycle of the tropical eastern Pacific sea surface
337 temperature, *Atmospheric Research*, 94(1), 3-9, doi:
338 10.1016/j.atmosres.2008.09.029.
- 339 An, S.-I., and H. Bong (2016), Inter-decadal change in El Nino-Southern Oscillation
340 examined with Bjerknes stability index analysis, *Climate Dynamics*, 47(3-4),
341 967-979, doi: 10.1007/s00382-015-2883-8.
- 342 An, S.-I., and J.-W. Kim (2017), Role of nonlinear ocean dynamic response to wind
343 on the asymmetrical transition of El Nino and La Nina, *Geophysical Research*
344 *Letters*, 44(1), 393-400, doi: 10.1002/2016gl071971.
- 345 Antonov, J. I., S. Levitus, and T. P. Boyer (2005), Thermosteric sea level rise,
346 1955-2003, *Geophysical Research Letters*, 32(12), doi: 10.1029/2005gl023112.
- 347 Antonov, J., Seidov, D., Boyer, T., Locarnini, R., Mishonov, A., Garcia, H., et al.
348 (2010). World ocean atlas 2009. In S. Levitus (Ed.), *Salinity* (Vol. 2, pp. 184).

349 Washington, DC: US Gov. Print. Off. Bleck, R. (2002), An oceanic general
350 circulation model framed in hybrid isopycnic-Cartesian coordinates, *Ocean*
351 *Modelling*, 4(1), 55-88, doi: 10.1016/s1463-5003(01)00012-9.

352 Becker, M., B. Meyssignac, C. Letetrel, W. Llovel, A. Cazenave, and T. Delcroix
353 (2012), Sea level variations at tropical Pacific islands since 1950, *Global and*
354 *Planetary Change*, 80-81, 85-98, doi: 10.1016/j.gloplacha.2011.09.004.

355 Burgers, G., and D. B. Stephenson (1999), The "normality" of El Nino, *Geophysical*
356 *Research Letters*, 26(8), 1027-1030, doi: 10.1029/1999gl900161.

357 Cazenave, A., and G. Le Cozannet (2014), Sea level rise and its coastal impacts,
358 *Earths Future*, 2(2), 15-34, doi: 10.1002/2013ef000188.

359 Cazenave, A., A. Lombard, and W. Llovel (2008), Present-day sea level rise: A
360 synthesis, *Comptes Rendus Geoscience*, 340(11), 761-770, doi:
361 10.1016/j.crte.2008.07.008.

362 Chang, Y.-T., L. Du, S.-W. Zhang, and P.-F. Huang (2013), Sea level variations in the
363 tropical Pacific Ocean during two types of recent El Nino events, *Global and*
364 *Planetary Change*, 108, 119-127, doi: 10.1016/j.gloplacha.2013.06.001.

365 Chen, L., Y. Jia, and Q. Liu (2015), Mesoscale eddies in the Mindanao Dome region,
366 *Journal of Oceanography*, 71(1), 133-140, doi: 10.1007/s10872-014-0255-3.

367 Cheng, X., Y. Qi, and W. Zhou (2008), Trends of sea level variations in the
368 Indo-Pacific warm pool, *Global and Planetary Change*, 63(1), 57-66, doi:
369 10.1016/j.gloplacha.2008.06.001.

370 Church, J. A., et al. (2013), Sea-Level Rise by 2100, *Science*, 342(6165), 1445-1445,

371 doi: 10.1126/science.342.6165.1445-a.

372 Dee, D. P., et al. (2011), The ERA-Interim reanalysis: configuration and performance
373 of the data assimilation system, *Quarterly Journal of the Royal Meteorological*
374 *Society*, 137(656), 553-597, doi: 10.1002/qj.828.

375 Duan, J., Y. Li, F. Wang, and Z. Chen (2019), Multidecadal Change of the Mindanao
376 Current: Is There a Robust Trend?, *Geophysical Research Letters*, 46(12),
377 6755-6764, doi: 10.1029/2019gl083090.

378 Gergis, J. L., and A. M. Fowler (2009), A history of ENSO events since AD 1525:
379 implications for future climate change, *Climatic Change*, 92(3-4), 343-387, doi:
380 10.1007/s10584-008-9476-z.

381 Xiao-li, G. U., and L. I. Pei-liang (2009), Pacific sea level variations and its factors,
382 *Acta Oceanologica Sinica*, 31(1), 28-36.

383 Hamlington, B. D., S. H. Cheon, P. R. Thompson, M. A. Merrifield, R. S. Nerem, R.
384 R. Leben, and K. Y. Kim (2016), An ongoing shift in Pacific Ocean sea level,
385 *Journal of Geophysical Research-Oceans*, 121(7), 5084-5097, doi:
386 10.1002/2016jc011815.

387 Im, S.-H., S.-I. An, S. T. Kim, and F.-F. Jin (2015), Feedback processes responsible
388 for El Nino-La Nina amplitude asymmetry, *Geophysical Research Letters*,
389 42(13), 5556-5563, doi: 10.1002/2015gl064853.

390 Jin, F. F. (1997), A theory of interdecadal climate variability of the North Pacific
391 ocean-atmosphere system, *Journal of Climate*, 10(8), 1821-1835, doi:
392 10.1175/1520-0442(1997)010<1821:atoicv>2.0.co;2.

393 Jin, F. F., J. S. Kug, S. I. An, and I. S. Kang (2003), A near-annual coupled
394 ocean-atmosphere mode in the equatorial Pacific ocean, *Geophysical Research*
395 *Letters*, 30(2), doi: 10.1029/2002gl015983.

396 Kang, I. S., and J. S. Kug (2002), El Nino and La Nina sea surface temperature
397 anomalies: Asymmetry characteristics associated with their wind stress
398 anomalies, *Journal of Geophysical Research-Atmospheres*, 107(D19), doi:
399 10.1029/2001jd000393.

400 Kang, I. S., and J. S. Kug (2000), An El-Nino prediction system using an intermediate
401 ocean and a statistical atmosphere, *Geophysical Research Letters*, 27(8),
402 1167-1170, doi: 10.1029/1999gl011023.

403 Kennedy, J. J., N. A. Rayner, R. O. Smith, D. E. Parker, and M. Saunby (2011),
404 Reassessing biases and other uncertainties in sea surface temperature
405 observations measured in situ since 1850: 2. Biases and homogenization, *Journal*
406 *of Geophysical Research-Atmospheres*, 116, doi: 10.1029/2010jd015220.

407 Le Traon, P. Y., F. Nadal, and N. Ducet (1998), An improved mapping method of
408 multisatellite altimeter data, *Journal of Atmospheric and Oceanic Technology*,
409 15(2), 522-534, doi: 10.1175/1520-0426(1998)015<0522:aimmom>2.0.co;2.

410 Li, Y., and W. Han (2015), Decadal Sea Level Variations in the Indian Ocean
411 Investigated with HYCOM: Roles of Climate Modes, Ocean Internal Variability,
412 and Stochastic Wind Forcing, *Journal of Climate*, 28(23), 9143-9165, doi:
413 10.1175/jcli-d-15-0252.1.

414 McCreary, J. (1976), Eastern Tropical Ocean Response to Changing Wind

415 System-with Application to El Nino, *Journal of Physical Oceanography*, 6(5),
416 632-645, doi: 10.1175/1520-0485(1976)006<0632:etortc>2.0.co;2.

417 Merrifield, M. A. (2011), A Shift in Western Tropical Pacific Sea Level Trends during
418 the 1990s, *Journal of Climate*, 24(15), 4126-4138, doi: 10.1175/2011jcli3932.1.

419 Milne, G. A., W. R. Gehrels, C. W. Hughes, and M. E. Tamisiea (2009), Identifying
420 the causes of sea-level change, *Nature Geoscience*, 2(7), 471-478, doi:
421 10.1038/ngeo544.

422 Nerem, R. S., D. P. Chambers, C. Choe, and G. T. Mitchum (2010), Estimating Mean
423 Sea Level Change from the TOPEX and Jason Altimeter Missions, *Marine*
424 *Geodesy*, 33, 435-446, doi: 10.1080/01490419.2010.491031.

425 Nicholls, R. J., and R. S. J. Tol (2006), Impacts and responses to sea-level rise: A
426 global analysis of the SRES scenarios over the twenty-first century, *Philos. Trans.*
427 *R. Soc. A Math. Phys. Eng. Sci.*, 364(1841), 1073–1095,
428 doi:10.1098/rsta-2006.1754.

429 Nicholls, R. J., P. P. Wong, V. R. Burkett, J. O. Codignotto, J. E. Hay, R. F. McLean, S.
430 Ragoonaden, and C. D. Woodroffe (2007), Coastal systems and low-lying areas,
431 in *Climate Change 2007: Impacts, Adaptation and Vulnerability. Fourth*
432 *Assessment Report of the Intergovernmental Panel on Climate Change (IPCC,*
433 *2007)*, edited by M. L. Parry, O. F. Canziani, J. P. Palutikof, P. J. van der Linden,
434 and C. E. Hanson, Cambridge University Press, Cambridge, UK. pp. 315–356.

435 Nicholls, R. J., and A. Cazenave (2010), Sea-level rise and its impact on coastal zones
436 (June, pg 1517, 2007), *Science*, 329(5992), 628-628.

437 Niedzielski, T., and W. Kosek (2010), El Nino's Impact on the Probability Distribution
438 of Sea Level Anomaly Fields, *Polish Journal of Environmental Studies*, 19(3),
439 611-620.

440 Ohba, M., and H. Ueda (2007), An impact of SST anomalies in the Indian ocean in
441 acceleration of the El Nino to La Nina transition, *Journal of the Meteorological*
442 *Society of Japan*, 85(3), 335-348, doi: 10.2151/jmsj.85.335.

443 Okumura, Y. M., and C. Deser (2010), Asymmetry in the Duration of El Nino and La
444 Nina, *Journal of Climate*, 23(21), 5826-5843, doi: 10.1175/2010jcli3592.1.

445 Qiu, B., and S. Chen (2010), Interannual-to-Decadal Variability in the Bifurcation of
446 the North Equatorial Current off the Philippines, *Journal of Physical*
447 *Oceanography*, 40(11), 2525-2538, doi: 10.1175/2010jpo4462.1.

448 Qiu, B., and S. Chen (2012), Multidecadal Sea Level and Gyre Circulation Variability
449 in the Northwestern Tropical Pacific Ocean, *Journal of Physical Oceanography*,
450 42(1), 193-206, doi: 10.1175/jpo-d-11-061.1.

451 Qiu, B., S. Chen, and H. Sasaki (2013), Generation of the North Equatorial
452 Undercurrent Jets by Triad Baroclinic Rossby Wave Interactions, *Journal of*
453 *Physical Oceanography*, 43(12), 2682-2698, doi: 10.1175/jpo-d-13-099.1.

454 Qiu, B., S. Chen, L. Wu, and S. Kida (2015), Wind- versus Eddy-Forced Regional Sea
455 Level Trends and Variability in the North Pacific Ocean, *Journal of Climate*,
456 28(4), 1561-1577, doi: 10.1175/jcli-d-14-00479.1.

457 Ren, Q., Y. Li, F. Wang, J. Duan, S. Hu, and F. Wang (2020), Variability of the
458 Mindanao Current Induced by El Niño Events, *Journal of Physical*

459 Oceanography, 0(0), null, doi: 10.1175/jpo-d-19-0150.1.

460 Palanisamy, H., A. Cazenave, T. Delcroix, and B. Meyssignac (2015), Spatial trend
461 patterns in the Pacific Ocean sea level during the altimetry era: the contribution
462 of thermocline depth change and internal climate variability, *Ocean Dynamics*,
463 65(3), 341-356, doi: 10.1007/s10236-014-0805-7.

464 Stammer, D., A. Cazenave, R. M. Ponte, and M. E. Tamisiea (2013), Causes for
465 Contemporary Regional Sea Level Changes, in *Annual Review of Marine
466 Science*, Vol 5, edited by C. A. Carlson and S. J. Giovannoni, pp. 21-46.

467 Su, J., R. Zhang, T. Li, X. Rong, J. S. Kug, and C.-C. Hong (2010), Causes of the El
468 Nino and La Nina Amplitude Asymmetry in the Equatorial Eastern Pacific,
469 *Journal of Climate*, 23(3), 605-617, doi: 10.1175/2009jcli2894.1.

470 Sverdrup, H. U. (1947), NOTE ON THE CORRECTION OF REVERSING
471 THERMOMETERS, *Journal of Marine Research*, 6(2), 136-138.

472 Wang, C. (2018), A review of ENSO theories, *National Science Review*, 5(6),
473 813-825, doi: 10.1093/nsr/nwy104.

474 Swerczynska, M., T. Niedzielski, and W. Kosek (2014), Semiannual and annual
475 oscillations of sea level and their impact on asymmetry between El Nino and La
476 Nina episodes, *Studia Geophysica Et Geodaetica*, 58(2), 302-325, doi:
477 10.1007/s11200-013-1124-z.

478 White, G. H. (1980), SKEWNESS, KURTOSIS AND EXTREME VALUES OF
479 NORTHERN HEMISPHERE GEOPOTENTIAL HEIGHTS, *Monthly Weather
480 Review*, 108(9), 1446-1455, doi:

481 10.1175/1520-0493(1980)108<1446:skaevo>2.0.co;2.

482 Wyrki, K. (1975), EL NINO - DYNAMIC-RESPONSE OF EQUATORIAL PACIFIC
483 OCEAN TO ATMOSPHERIC FORCING, Journal of Physical Oceanography,
484 5(4), 572-584, doi: 10.1175/1520-0485(1975)005<0572:entdro>2.0.co;2.

485 Yu, J. Y., C. R. Mechoso, and S. O. C. Amer Meteorol (1997), On the asymmetry of
486 SST in the tropical Pacific, 613-614 pp.

487 Zebiak, S. E. (1989), OCEANIC HEAT-CONTENT VARIABILITY AND EL NINO
488 CYCLES, Journal of Physical Oceanography, 19(4), 475-486, doi:
489 10.1175/1520-0485(1989)019<0475:ohcvac>2.0.co;2.

490 Zhang, X., and J. A. Church (2012), Sea level trends, interannual and decadal
491 variability in the Pacific Ocean, Geophysical Research Letters, 39(21), doi:
492 10.1029/2012gl053240.

493

494 **Figure captions**

495 **Figure 1.** Standard deviation (STD) of sea level anomalies (SLAs, m) of 1993-2016
496 from (a) AVISO sea level product and (b) HYCOM-CTL. (c) Skewness of SLAs. (d)
497 Regression coefficient $k_{\text{Niño}}$ (m) of SLAs onto the normalized Niño-3.4 index for El
498 Niño condition (Niño-3.4 > 0). (e) Same as (b) but for La Niña condition (Niño-3.4 <
499 0). (f) Ratio of $k_{\text{Niño}}$ to $k_{\text{Niña}}$, i.e., $R_k = k_{\text{Niño}}/k_{\text{Niña}}$. SLA data in (c)-(f) are derived from
500 AVISO sea level product of 1993-2016.

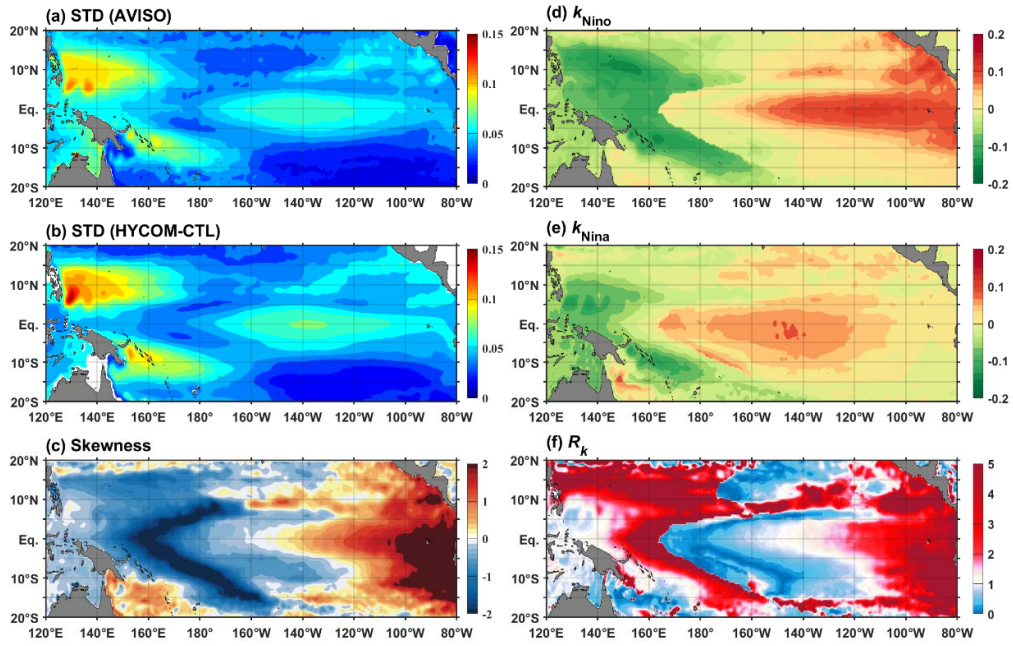
501 **Figure 2.** R_k distributions during 1993-2016 simulated by (a) HYCOM-CTL, (b)
502 HYCOM-TAU, and (c) RGO-CTL. (d)-(f) are the same as (a)-(c), but for the
503 1979-2016 period.

504 **Figure 3.** R_k distributions from (a) EXP1, (b) EXP2, (c) EXP1-TAUX and (d)
505 EXP2-TAUX. (e) and (f) show the 1st singular value decomposition (SVD) modes for
506 zonal wind stress τ^x (N m^{-2} ; solid and dashed contours for positive and negative
507 values) and upper-layer thickness ULT (m; color shading) of EXP1-TAUX1 for El
508 Niño and La Niña conditions, respectively.

509 **Figure 4.** (a) Zonal structure of the 5°S-5°N average τ^x (left), and ULT (middle) of
510 the 1st SVD mode, and regression coefficients ($k_{\text{Niño}}$ and $k_{\text{Niña}}$; right) in EXP1-TAUX,
511 computed separated for the for El Niño and La Niña conditions. (b) Same as (a) but
512 for EXP2-TAUX. (c) is the same as (a), but for τ^x of the 1st SVD mode in
513 RGO-CTL, and theoretically-predicted ULT and regression coefficients (see the text
514 for details), and they are normalized by the standard deviation.

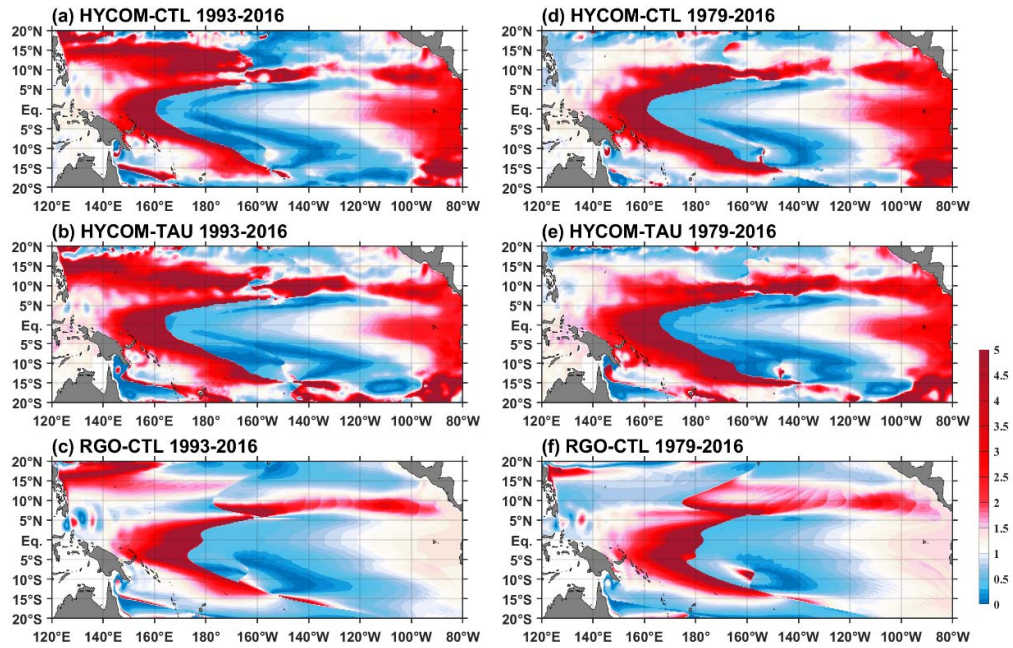
515

516 **Figures**



517

518 **Figure 1.** Standard deviation (STD) of sea level anomalies (SLAs, m) of 1993-2016
 519 from (a) AVISO sea level product and (b) HYCOM-CTL. (c) Skewness of SLAs. (d)
 520 Regression coefficient k_{Nino} (m) of SLAs onto the normalized Niño-3.4 index for El
 521 Niño condition ($Ni\tilde{no}-3.4 > 0$). (e) Same as (b) but for La Niña condition ($Ni\tilde{no}-3.4 <$
 522 0). (f) Ratio of k_{Nino} to k_{Nina} , i.e., $R_k = k_{Nino}/k_{Nina}$. SLA data in (c)-(f) are derived from
 523 AVISO sea level product of 1993-2016.

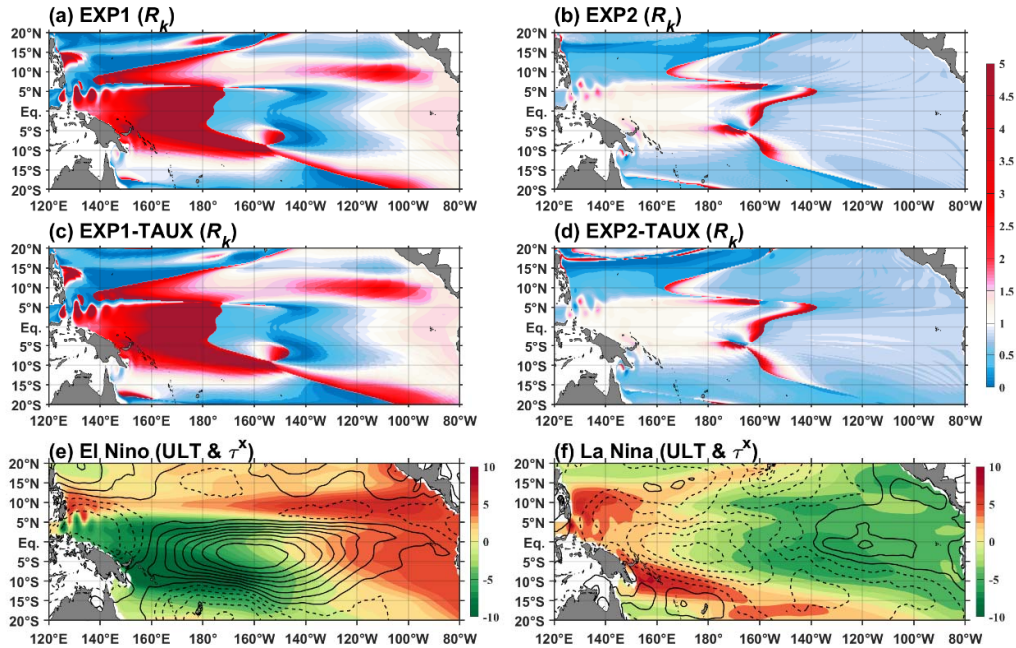


524

525 **Figure 2.** R_k distributions during 1993-2016 simulated by (a) HYCOM-CTL, (b)

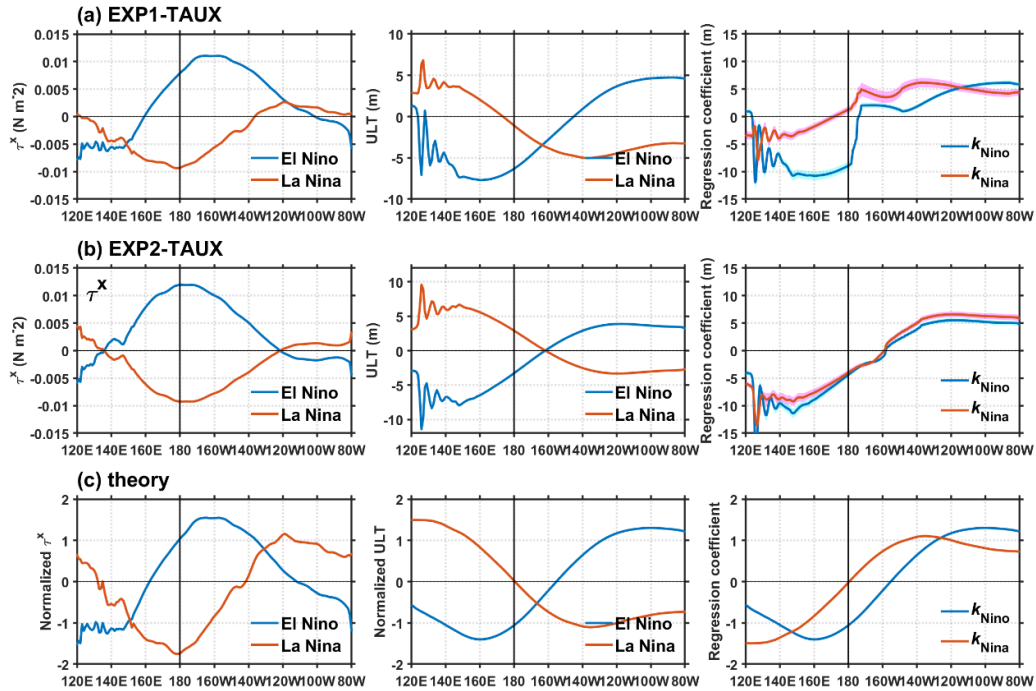
526 HYCOM-TAU, and (c) RGO-CTL. (d)-(f) are the same as (a)-(c), but for the

527 1979-2016 period.



528

529 **Figure 3.** R_k distributions from (a) EXP1, (b) EXP2, (c) EXP1-TAUX and (d)
 530 EXP2-TAUX. (e) and (f) show the 1st singular value decomposition (SVD) modes for
 531 zonal wind stress τ^x (N m^{-2} ; solid and dashed contours for positive and negative
 532 values) and upper-layer thickness ULT (m; color shading) of EXP1-TAUX1 for El
 533 Niño and La Niña conditions, respectively.



534

535 **Figure 4.** (a) Zonal structure of the 5°S-5°N average τ^x (left), and ULT (middle) of
 536 the 1st SVD mode, and regression coefficients (k_{Nino} and k_{Nina} ; right) in EXP1-TAUX,
 537 computed separated for the for El Niño and La Niña conditions. (b) Same as (a) but
 538 for EXP2-TAUX. (c) is the same as (a), but for τ^x of the 1st SVD mode in
 539 RGO-CTL, and theoretically-predicted ULT and regression coefficients (see the text
 540 for details), and they are normalized by the standard deviation.

Submitted to *Geophysical Research Letters*

Asymmetric Responses of the Western Tropical Pacific Sea Level to El Niño and La Niña

Qiuping Ren^{1,2}, Yuanlong Li^{1,3,4}, Fei Zheng^{3,5}, Fan Wang^{1,2,3,4,*},
Jing Duan^{1,3,4}

¹Key Laboratory of Ocean Circulation and Waves, Institute of Oceanology, Chinese Academy of Sciences, Qingdao, China,

²University of Chinese Academy of Sciences, Beijing, China,

³Center for Ocean Mega-Science, Chinese Academy of Sciences, Qingdao, China,

⁴Function Laboratory for Ocean Dynamics and Climate, Qingdao National Laboratory for Marine Science and Technology, Qingdao, China,

⁵International Center for Climate and Environment Science, Institute of Atmospheric Physics, Chinese Academy of Sciences, Beijing, China,

April 2020

***Corresponding Author:**

Fan Wang

Key Laboratory of Ocean Circulation and Waves, Institute of Oceanology, Chinese Academy of Sciences, Qingdao 266071, China.

Email: fwang@qdio.ac.cn

1 **Key Points.**

- 2 1) The responses of the western tropical Pacific sea level to ENSO are
3 obviously asymmetric, and the response to El Niño is evidently stronger.
- 4 2) The different surface wind anomaly structure between El Niño and La Niña
5 is critical for the asymmetric response of sea level.
- 6 3) The asymmetric ocean responses to ENSO may contribute to the ENSO
7 asymmetry.

8 **Abstract**

9 The western tropical Pacific (WTP) exhibits large interannual sea level
10 anomalies (SLAs), and the sea level falling in El Niño is evidently stronger than the
11 rising in La Niña. The asymmetry is most prominent near 160°E with the response to
12 El Niño larger by three times and becomes less obvious near the western boundary.
13 Sensitivity experiments of a simplified ocean model suggest that the asymmetry in
14 surface wind forcing structure between El Niño and La Niña is critical. The El Niño's
15 westerly wind anomaly patch locates more east than the La Niña's easterly wind patch
16 during the mature stage, and its upwelling effects are accumulated over a wider
17 longitude range and cause stronger negative SLAs in the WTP. Near the western
18 boundary, however, upwelling effects are attenuated by easterly wind anomalies
19 during El Niño conditions. The asymmetric ocean responses to ENSO winds may
20 participate in the asymmetry of ENSO cycle.

21 **Plain Language Summary**

22 El Niño–Southern Oscillation (ENSO) is the most influential climate variability
23 mode of the Pacific and cause strong interannual sea level anomalies (SLAs) in the
24 western tropical Pacific (WTP). We notice that the WTP's sea level falling in El Niño
25 condition is stronger than its sea level rising in La Niña. This difference is most
26 prominent near 160°E, where the falling in El Niño is stronger by three times. This
27 phenomenon becomes much less evident near the western boundary of the Pacific
28 basin. We further show that the difference in surface wind anomaly structures between
29 El Niño and La Niña is the primary cause. El Niño's westerly wind anomaly center

30 locates more east than La Niña's easterly wind anomaly center in their mature phase,
31 and there are easterly wind anomalies emerging near the western boundary during El
32 Niño condition. As a result, effect of El Niño's westerly wind anomaly is accumulated
33 over a wider longitude range and causes stronger sea level falling in the WTP. But this
34 effect becomes weaker near the western boundary, due to easterly wind anomalies
35 there. By contrast, effect of La Niña's easterly wind anomaly strengthens
36 monotonically from east to west, but the produced sea level rising signatures are
37 mainly confined to the WTP.

38 **Keywords**

39 Western Tropical Pacific, Sea Level, ENSO, ENSO asymmetry, Interannual

40 Variability

41 **1. Introduction**

42 Regional sea level change, as an essential aspect of climate change, is attracting
43 increasing attention of scientific communities and the general public, because of its
44 threats on eco-systems and people of coastal residence (e.g., Nicholls & Cazenave,
45 2010; Cazenave & Cozannet, 2014). There is a paramount demand for improved
46 understanding of regional sea level changes on various timescales (e.g., Milne et al.,
47 2009; Church et al., 2013; Stammer et al., 2013). Sea level changes over the tropical
48 Pacific Ocean are particularly pronounced on interannual timescale, as largely
49 modulated by El Niño-Southern Oscillation (ENSO) (e.g., Cazenave et al., 2008;
50 Antonov et al., 2005; Cheng et al., 2008). It is evident in Figure 1a that the western
51 tropical Pacific (WTP) shows stronger interannual sea level anomalies (SLAs) than
52 other regions, as quantified the standard deviation of low-passed SLAs. The WTP
53 shows strong sea level rising (falling) during the La Niña (El Niño) condition, as a
54 result of prevailing easterly (westerly) wind anomalies over the tropical Pacific basin
55 (Wyrtki, 1975; Zebiak, 1984; Alory & Delcroix, 2002; Gu & Li, 2009; Nerem et al.,
56 2010; Merrifield, 2011; Zhang & Church, 2012; Chang et al., 2013; Becker et al.,
57 2016; Hamlington et al., 2016). The sea level rising during La Niña conditions is
58 expected to aggravate coastal erosion, extreme marine flooding, or saltwater intrusion
59 in coastal aquifers (Nicholls & Tol, 2006; Nicholls et al., 2007; Nicholls & Cazenave,
60 2010), thus becomes a major threat for the densely populated coastal regions.
61 However, the sea level falling during El Niño causes the coral reef exposure and could
62 damage the region's ecosystem. There are many heavily-populated coasts and islands

63 in the WTP, so the sea level changes during ENSO are well worth studying.

64 El Niño and La Niña are, however, not mirrors of each other. They exhibit
65 obvious asymmetry in magnitude, duration time, and occurrence frequency (e.g.,
66 Burgers & Stephenson, 1999; Ohba & Ueda, 2007; Gergis & Fowler, 2009; An &
67 Choi, 2009; Okumura & Deser, 2010). Their signatures on sea level are also
68 asymmetric, owing to not only ENSO's asymmetry but also the nonlinearity in ocean
69 response (Niedzielski & Kosek, 2010; Swierczynska et al., 2013; Im et al., 2015; An
70 & Kim, 2017). Previous studies have demonstrated that ENSO asymmetry is
71 contributed by nonlinear dynamical heating of ocean current advection (e.g., Kang &
72 Kug, 2002; Jin et al., 2003; An & Jin, 2004; Su et al., 2010). As dynamically
73 associated with the upper-ocean currents through pressure gradient, the asymmetric
74 SLAs induced by ENSO may affect ocean current advection of heat and thereby
75 participate in the ENSO asymmetry.

76 In this study, we aim to investigate the asymmetric response of the WTP sea
77 level to ENSO and the underlying dynamical processes. This effort is of paramount
78 need for the prediction and projection of regional sea level change and adaptations of
79 the low-lying coasts and islands, as well as for understanding the dynamics of ENSO
80 asymmetry. The rest of the paper is structured as follows. Section 2 describes the data
81 and models. Section 3 describes the asymmetric SLAs of the WTP in response to
82 ENSO. Section 4 explores the underlying dynamics through a simplified ocean model.
83 Section 5 presents concluding remarks.

84 **2. Data and Models**

85 **2.1. Data**

86 In this study we use $0.25^\circ \times 0.25^\circ$, monthly satellite SLA data of 1993-2016
87 from Archiving Validation, and Interpretation of Satellite Oceanography (AVISO; Le
88 Traon et al., 1998) and sea level records of three tidal gauge stations in the WTP:
89 Malakal at 7.33°N , 134.45°E for 1979-2016, Kapingamrangi at 1.1°N , 154.78°E for
90 1929-2016, and Lombrum at 2.04°S , 147.47°E for 1995-2016 (Figure S1 in the
91 Supporting Information). The Hadley Centre Sea Ice and Sea Surface Temperature
92 (HadISST) data set (Kennedy et al., 2011) of the Met Office during 1979-2016 with
93 horizontal resolution of $1^\circ \times 1^\circ$ is used to compute Niño-3.4 index and identify El
94 Niño and La Niña conditions. Surface winds and other surface atmospheric fields of
95 1979-2016 are taken from the 0.75° monthly dataset of the European Centre for
96 Medium-Range Weather Forecasts (ECMWF) ERA-interim (Dee et al., 2011).

97 **2.2. HYCOM**

98 The HYbrid Coordinate Ocean Model (HYCOM) version 2.2.18 (Bleck, 2002)
99 are used to simulate interannual SLAs in the tropical Pacific Ocean. HYCOM is
100 configured to the Pacific Ocean basin between 48°S - 48°N , 110°E - 70°W , with a
101 horizontal resolution of $1/3^\circ \times 1/3^\circ$ and 26 hybrid vertical layers (Li et al., 2015; Ren et
102 al., 2020). Surface atmospheric forcing fields (winds, heat fluxes, precipitation, etc.)
103 are taken from ERA-interim. Three sponge layers are applied to the western, southern
104 and northern open-ocean boundaries, where model temperature and salinity are
105 related to the World Ocean Atlas 2009 (WOA09) climatology (Antonov et al., 2010).

106 More details of model configuration are described in Ren et al. (2020). Subsequent to
107 the spin-up run of 30 years under monthly climatologic forcing, two parallel
108 experiments are performed under daily ERA-Interim fields for the period of 1979-
109 2016. The control run (HYCOM-CTL) is forced with the original daily atmospheric
110 fields and assumed to contain the complete processes. This experiment can well
111 reproduce the amplitude and spatial distribution of interannual SLA and upper-ocean
112 circulation variation in observation (Figure 1b; Ren et al., 2020). Another experiment,
113 HYCOM-TAU, uses daily wind stress forcing as HYCOM-CTL, but all the other
114 forcing fields (heat and freshwater fluxes) are fixed to monthly climatology.
115 HYCOM-TAU is used to evaluate the effects of wind forcing on sea level.

116 **2.3. Reduced-Gravity Ocean Model**

117 To achieve more in-depth understanding, a series of experiments are performed
118 with a 1.5-layer nonlinear reduced-gravity ocean (RGO) model. This model mainly
119 represents the 1st-mode baroclinic response of the ocean to surface wind forcing,
120 which is the dominant source of large-scale interannual variability in sea level and
121 upper-ocean circulation of the WTP (e.g., Qiu & Chen, 2010, 2012). The model is
122 configured to the Pacific Ocean basin between 40°S-40°N, 100°E-70°W with
123 horizontal resolutions of 0.25°×0.25° and forced by monthly ERA-Interim surface
124 winds. Readers are referred to Duan et al. (2019) for more details of the model
125 configuration. After a spin-up of 10 years under climatological wind forcing, the
126 control run of RGO model (RGO-CTL) is forced by realistic monthly winds. RGO
127 model experiments (Table S1) are forced by idealized wind forcing to examine the

128 role of wind forcing asymmetry and are described in Section 4.

129 **3. Asymmetric Responses to El Niño and La Niña**

130 To highlight the interannual variations associated with ENSO, we analyze the 13-
131 month low-pass filtered anomaly fields with the monthly climatology removed.

132 Skewness S is a measure of the distribution asymmetry with $S = 0$ indicating a normal
133 distribution (White, 1980). Figure 1c shows the skewness of the observed SLA over
134 the tropical Pacific for 1993-2016. The eastern tropical Pacific is positively skewed
135 with the maximum S of ~ 2.0 , while the central-western tropical Pacific is negatively
136 skewed with the minimum S of -2.0 and a horseshoe structure extending from the
137 equator to extratropical regions in both hemispheres. This distribution of SLA
138 skewness resembles that of SST anomaly (An & Jin, 2004; Niedzielski & Kosek,
139 2010) and is likely associated with the positive skewness of ENSO (Nerem et al.,
140 2010). The El Niño condition is characterized by positive SLAs in the eastern Pacific
141 and negative SLAs in the WTP, and these anomalies are stronger in amplitude than
142 the opposite SLAs occurring in La Niña condition (Niedzielski & Kosek, 2010;
143 Figure S1).

144 In addition to the asymmetry residing in ENSO (e.g., as quantified by the
145 skewness of Niño-3.4 index), the asymmetric responses of sea level to El Niño and La
146 Niña also contribute to the SLA asymmetry shown in Figure 1c. We regress SLAs
147 onto the normalized Niño-3.4 index separately for the El Niño condition (Niño-3.4 >
148 0) and the La Niña condition (Niño-3.4 < 0). The corresponding regression
149 coefficients, namely $k_{\text{Niño}}$ and $k_{\text{Niña}}$, are used to quantify the responses of SLA to El

150 Niño and La Niña, respectively (Figures 1d and 1e). The response time of sea level to
151 ENSO shows spatial variation, as indicated by the lead-lag correlation (Figure S2a).
152 For each grid point, the lead-lag time of the maximal correlation is used to compute
153 the regression coefficient. The results are not dramatically different from those of
154 simultaneous regression (Figure S2b). Figures 1d and 1e show distributions of k_{Nino}
155 and k_{Nina} . In the WTP, the maximal k_{Nino} of ~ -0.2 m is located 20° - 30° away from the
156 western boundary, and k_{Nino} decreases in magnitude as approaching the western
157 boundary. By contrast, the peak k_{Nina} values of ~ -0.15 m are close to the western
158 boundary. We further use the ratio of k_{Nino} to k_{Nina} to quantify the response asymmetry,
159
$$R_k = \frac{k_{Nino}}{k_{Nina}}. \quad (1)$$

160 $R_k = 1$ denotes symmetric response of SLAs to El Niño and La Niña, while $R_k > 1$ and
161 $R_k < 1$ indicates stronger and weaker response to El Niño than to La Niña,
162 respectively. As shown in Figure 1f, R_k reaches the largest value near 160° E with
163 values exceeding 3.0, indicating that the response of SLA to El Niño is stronger by at
164 least 3 times than the response to La Niña. R_k is weakened to ~ 1.0 near the western
165 boundary, implying SLA responses there are nearly symmetric. This interesting
166 distribution of R_k in the WTP and underlying dynamics are worthy of systematic
167 investigation. One may notice that R_k is < 1 in the central Pacific and is > 1 in the
168 eastern Pacific, indicative of prevailing asymmetry over the tropical Pacific basin. In
169 the following, we focus on explaining the R_k distribution in the WTP.

170 Simulations of HYCOM and RGO model have faithfully reproduced the
171 observed interannual variations of sea level at three tidal gauge stations (Figure S3).

172 The upper-layer thickness (ULT) anomaly of the 1.5-layer RGO model is a good
173 proxy of SLA in the tropical Pacific (e.g., Qiu & Chen, 2010, 2012; Chang et al.,
174 2013; Duan et al., 2019). The correlations among AVISO, HYCOM-CTL, HYCOM-
175 TAU and RGO-CTL at the three tidal gauge stations are all above 0.85. The
176 asymmetric responses of SLAs to El Niño and La Niña in the WTP during 1993-2016
177 can be realistically reproduced by HYCOM-CTL, HYCOM-TAU, and RGO-CTL
178 (Figures 2a-2c), although RGO-CTL fails to capture the features in the eastern
179 Pacific. The good performance of HYCOM-TAU and RGO-CTL indicates that the
180 interannual SLAs in the WTP and their asymmetric features are primarily the results
181 of ENSO wind forcing, and the underlying dynamics can be explored by sensitive
182 model experiments with prescribed wind forcing fields.

183 **4. Dynamics**

184 To include more ENSO events, we use the period of 1979-2016 to perform
185 model experiments (Table S1), although R_k of 1979-2016 shows detailed differences
186 from that of 1993-2016 in the northwest Pacific (Figures 2d-2f). According to existing
187 studies of ENSO asymmetry, the different spatial and temporal characteristics of wind
188 anomalies are essential to cause the SST asymmetry between El Niño and La Niña
189 (Kang & Kug, 2002; An & Kim, 2017). To examine which aspect of ENSO's wind
190 forcing is critical in regulating the asymmetric responses of SLAs, we adopt a
191 statistical model based on the singular value decomposition (SVD) of wind stress and
192 SST (Kang & Kug, 2000), which is expressed as

$$193 \quad \boldsymbol{\tau}'(x, y, t) = \sum_n^N c(n) [\sum_{x,y} V_{\text{SST}}(x, y, n) T(x, y, t)] V_{\boldsymbol{\tau}}(x, y, n), \quad (2)$$

194 where x , y , and t represent longitude, latitude, and time, respectively, V_{SST} and V_{τ} are
 195 the SVD singular vectors for SST and wind stress, T is the SST anomaly field, and n
 196 $= 1, 2, \dots, N$ indicates the n th mode of SVD, $\sum_{x,y}$ indicates spatial integration over
 197 the region of 100° - 290° E, 40° S- 40° N. $c(n)$ represents the correlation between SST
 198 and wind stress anomalies,

$$199 \quad c(n) = \frac{\sum_t t_{\text{SST}}(t,n)t_{\tau}(t,n)}{\sum_t t_{\text{SST}}(t,n)^2}, \quad (3)$$

200 where t_{SST} and t_{τ} are the corresponding time series, the numerator is the covariance
 201 of t_{SST} and t_{τ} and the denominator is the variance of t_{SST} , and \sum_t indicates temporal
 202 integration from January 1979 to December 2016. Zonal and meridional components
 203 of τ' are separately computed. All the RGO sensitive experiments are forced by
 204 monthly wind stress anomalies constructed by Eq. 2 (representing ENSO wind
 205 forcing) plus monthly climatological winds.

206 We first perform two experiments, namely EXP1 and EXP2. EXP1 uses different
 207 wind stress anomaly fields for El Niño and La Niña conditions. Specifically, $\tau'_{\text{Niño}}$ and
 208 $\tau'_{\text{Niña}}$ are reconstructed separated for Niño-3.4 ≥ 0 and Niño-3.4 < 0 conditions
 209 (Figures S4a and S4b) using Eq. 2, respectively, so that the synthesized τ' still retains
 210 the difference in spatial structure between El Niño and La Niña conditions. By
 211 contrast, EXP2 does not distinguish El Niño and La Niña conditions and uses
 212 reconstructed τ' for the entire model period (Figure S4c). As such, the difference
 213 between EXP1 and EXP2 represents the effect of different wind anomaly structures
 214 between El Niño and La Niña on SLAs. In EXP1 and EXP2, we use only the leading
 215 mode ($n = 1$) of SVD to reconstruct τ' (Figure S4), which explains $> 85\%$ of the total

216 covariance and mainly represents ENSO's mature phase (Figure S5). The higher SVD
217 modes largely represent the transition stages between El Niño and La Niña polarities
218 (Figure S5) and have limited impacts on the asymmetry of SLAs (Figure S6).

219 Figures 3a and 3b show R_k distributions of ULT produced by EXP1 and EXP2,
220 respectively. EXP1 is able to reproduce large R_k values in the WTP as RGO-CTL,
221 whereas R_k is generally close to 1.0 in EXP2. These results suggest that the
222 asymmetry in surface wind structures between El Niño and La Niña is largely
223 responsible for asymmetric responses of the WTP sea level. Note that EXP2 still
224 retains some asymmetric characteristics of ENSO winds, such as the asymmetries in
225 intensity, frequency, and temporal evolution. Figure 3b however indicates that these
226 factors have little contributions to SLA asymmetry. This is confirmed by an additional
227 experiment EXP3, which adopts an idealized sine time series for τ' (Table S1) and
228 achieves similar results to EXP2 (Figure S7).

229 In the equatorial zone, zonal component of wind stress τ^x is much more
230 influential for the ocean than the meridional component. We repeat EXP1 and EXP2
231 using only τ^x anomaly, and τ^y is fixed to monthly climatology (EXP1-TAUX and
232 EXP2-TAUX). The results of two experiments achieve are broadly consistent with
233 EXP1 and EXP2 (Figures 3c and 3d). Therefore, the spatial structure of τ^x is critical
234 for the asymmetric responses. The typical structures of ULT and τ^x in EXP1-TAUX
235 for warm and cold phases are shown in Figures 3e and 3f, respectively, as represented
236 by the leading SVD mode of τ^x and ULT. Notice that westerly wind anomaly patch of
237 El Niño locates more east than the easterly wind anomaly patch of La Niña in their

238 mature phase, and correspondingly the zero value of ULT anomaly of El Niño also
 239 locates more east (Jin, 1997; Kang & Kug, 2002). During El Niño there are easterly
 240 wind anomalies near the western boundary. The strong negative ULT anomalies in El
 241 Niño are seen over a wide longitude range and weaken as approaching the western
 242 boundary, while the positive ULT anomalies in La Niña are confined to the far WTP
 243 and generally strengthen westward.

244 To better elucidate how the wind forcing structure cause asymmetric SLAs, we
 245 show in Figure 4 the zonal distributions of τ^x and ULT in the equatorial band (5°S-
 246 5°N). It is clearly discernible in Figure 4a that the El Niño's westerly wind anomaly
 247 patch locates more east than the La Niña's easterly wind anomaly patch. The forcing
 248 effect of equatorial zonal wind stress on sea level and ULT slopes can be roughly
 249 expressed in a linear relationship (Sverdrup, 1947; McCreary, 1977; Alory &
 250 Delcroix, 2002; Palanisamy et al., 2014),

$$251 \quad \frac{dh}{dx} = \tau^x, \quad (4)$$

252 where h is ULT anomaly or SLA. Therefore, $h(x)$ at a given longitude x can be
 253 determined by the integration of Eq. (4) from the eastern boundary $x_E = 70^\circ\text{W}$ along
 254 equator,

$$255 \quad h(x) = h(x_E) + \int_{x_E}^x \tau^x dx. \quad (5)$$

256 Since $h(x_E)$ diffuses quickly away from the eastern boundary as free Rossby waves
 257 and has little impact on the interior Pacific (Qiu et al., 2013), $h(x)$ is primarily
 258 determined by the zonal integral of τ^x from x_E to x (second term). As such, the
 259 negative ULT anomaly in El Niño in the WTP is much stronger than the positive ULT

260 anomaly in La Niña owing to the much wider westerly wind anomaly patch to its east.
 261 West of 160°E, easterly wind anomaly near the western boundary causes downwelling
 262 of the ocean, resulting in the attenuation of negative ULT anomalies there. By
 263 contrast, the La Niña's positive ULT anomalies are continuously strengthened by
 264 easterly wind anomalies. As a result, the ULT anomalies of El Niño and La Niña are
 265 comparable in amplitude in the far WTP, and the asymmetry of response is no longer
 266 evident there (right panel of Figure 4a). In EXP2-TAUX (Figure 4b), without the
 267 difference in wind forcing structure (left panel), the asymmetric responses cannot be
 268 reproduced (middle and right panels).

269 Figure 4c shows the zonal distributions of ULT anomaly and regression
 270 coefficients predicted by the linear theory, which compare favorably with Figure 4a. It
 271 indicates that the linear theory can to a large extent capture the processes causing
 272 asymmetric responses to ENSO winds and confirms the critical role played by the
 273 structure of zonal wind anomaly. Under this theoretical framework, the response
 274 asymmetry R_k can be theoretically expressed as,

$$275 \quad R_k(x) \approx \frac{\int_{x_E}^x \tau^x_{Nino} dx}{\int_{x_E}^x \tau^x_{Nina} dx}, \quad (6)$$

276 where τ^x_{Nino} and τ^x_{Nina} are the zonal wind stress anomaly in El Niño and La Niña
 277 conditions, respectively. Eq. (6) clearly suggests the sensitivity of $R_k(x)$ to the
 278 distribution of τ^x from x to the eastern boundary.

279 **5. Concluding Remarks**

280 The WTP exhibits large interannual variations of sea level, and the sea level

281 falling in El Niño is stronger than the rising in La Niña. Here we show that this
282 asymmetry is most prominent near 160°E with the response to El Niño larger by ~3
283 times and becomes much less obvious near the western boundary. RGO model
284 experiments suggest that the asymmetric surface wind anomaly structure between El
285 Niño and La Niña conditions is critical. El Niño's westerly wind anomaly patch
286 locates more east than La Niña's easterly wind anomaly patch in their mature stages.
287 As such, the upwelling effects of westerly wind anomalies are accumulated over a
288 wider longitude range and cause stronger negative SLAs in the WTP. As approaching
289 further toward the western boundary, positive SLAs in La Niña continue to amplify,
290 while negative SLAs of El Niño are attenuated by easterly wind anomalies in the far
291 WTP.

292 Here we reveal the sensitivity of the asymmetric SLAs in the WTP to the ENSO
293 wind structures. It is interesting to investigate whether the asymmetric SLAs in turn
294 contributes to the ENSO asymmetry in amplitude and temporal evolutions. This can
295 be investigated through careful heat budget analysis that evaluate the effects of
296 asymmetric current advection on SST variability. In addition, the zonal surface wind
297 patch dominates the SLA asymmetry along the equator, and its off-equatorial structure
298 may affect the asymmetry beyond the equator by modifying the wind stress curl (An
299 & Bong, 2016). In addition to wind forcing, the effects of local nonlinear processes,
300 such as mesoscale eddies, on sea level in the WTP are not resolved by the RGO
301 model experiments (Chen et al., 2015; Qiu et al., 2015), which can be also examined
302 in the future study.

303 **Acknowledgments**

304 This research is supported by National Natural Science Foundation of China
305 (grants 41730534 and 41806014) and the National Program on Global Change and Air-
306 Sea Interaction (grant GASI-IPOVAI-01-01). AVISO sea level data are available at
307 <http://marine.copernicus.eu/services-portfolio/access-to-products/>. Tidal gauges data
308 are available at <https://www.psmsl.org/>. ERA-Interim wind data are available at
309 <https://apps.ecmwf.int/datasets/>. HadISST data are downloaded from Met-Office
310 website <https://www.metoffice.gov.uk/hadobs/>.

311

312 **References**

- 313 Alory, G., and T. Delcroix (2002), Interannual sea level changes and associated mass
314 transports in the tropical Pacific from TOPEX/Poseidon data and linear model
315 results (1964-1999), *Journal of Geophysical Research-Oceans*, 107(C10), doi:
316 10.1029/2001jc001067.
- 317 An, S. I., and F. F. Jin (2004), Nonlinearity and asymmetry of ENSO, *Journal of*
318 *Climate*, 17(12), 2399-2412, doi: 10.1175/1520-
319 0442(2004)017<2399:naaoe>2.0.co;2.
- 320 An, S.-I., and J. Choi (2009), Seasonal locking of the ENSO asymmetry and its
321 influence on the seasonal cycle of the tropical eastern Pacific sea surface
322 temperature, *Atmospheric Research*, 94(1), 3-9, doi:
323 10.1016/j.atmosres.2008.09.029.
- 324 An, S.-I., and H. Bong (2016), Inter-decadal change in El Nino-Southern Oscillation
325 examined with Bjerknes stability index analysis, *Climate Dynamics*, 47(3-4),
326 967-979, doi: 10.1007/s00382-015-2883-8.
- 327 An, S.-I., and J.-W. Kim (2017), Role of nonlinear ocean dynamic response to wind
328 on the asymmetrical transition of El Nino and La Nina, *Geophysical Research*
329 *Letters*, 44(1), 393-400, doi: 10.1002/2016gl071971.
- 330 Antonov, J. I., S. Levitus, and T. P. Boyer (2005), Thermosteric sea level rise, 1955-
331 2003, *Geophysical Research Letters*, 32(12), doi: 10.1029/2005gl023112.
- 332 Antonov, J., Seidov, D., Boyer, T., Locarnini, R., Mishonov, A., Garcia, H., et al.
333 (2010). World ocean atlas 2009. In S. Levitus (Ed.), *Salinity* (Vol. 2, pp. 184).

334 Washington, DC: US Gov. Print. Off. Bleck, R. (2002), An oceanic general
335 circulation model framed in hybrid isopycnic-Cartesian coordinates, *Ocean*
336 *Modelling*, 4(1), 55-88, doi: 10.1016/s1463-5003(01)00012-9.

337 Becker, M., B. Meyssignac, C. Letetrel, W. Llovel, A. Cazenave, and T. Delcroix
338 (2012), Sea level variations at tropical Pacific islands since 1950, *Global and*
339 *Planetary Change*, 80-81, 85-98, doi: 10.1016/j.gloplacha.2011.09.004.

340 Burgers, G., and D. B. Stephenson (1999), The "normality" of El Nino, *Geophysical*
341 *Research Letters*, 26(8), 1027-1030, doi: 10.1029/1999gl900161.

342 Cazenave, A., and G. Le Cozannet (2014), Sea level rise and its coastal impacts,
343 *Earths Future*, 2(2), 15-34, doi: 10.1002/2013ef000188.

344 Cazenave, A., A. Lombard, and W. Llovel (2008), Present-day sea level rise: A
345 synthesis, *Comptes Rendus Geoscience*, 340(11), 761-770, doi:
346 10.1016/j.crte.2008.07.008.

347 Chang, Y.-T., L. Du, S.-W. Zhang, and P.-F. Huang (2013), Sea level variations in the
348 tropical Pacific Ocean during two types of recent El Nino events, *Global and*
349 *Planetary Change*, 108, 119-127, doi: 10.1016/j.gloplacha.2013.06.001.

350 Chen, L., Y. Jia, and Q. Liu (2015), Mesoscale eddies in the Mindanao Dome region,
351 *Journal of Oceanography*, 71(1), 133-140, doi: 10.1007/s10872-014-0255-3.

352 Cheng, X., Y. Qi, and W. Zhou (2008), Trends of sea level variations in the Indo-
353 Pacific warm pool, *Global and Planetary Change*, 63(1), 57-66, doi:
354 10.1016/j.gloplacha.2008.06.001.

355 Church, J. A., et al. (2013), Sea-Level Rise by 2100, *Science*, 342(6165), 1445-1445,

356 doi: 10.1126/science.342.6165.1445-a.

357 Dee, D. P., et al. (2011), The ERA-Interim reanalysis: configuration and performance
358 of the data assimilation system, *Quarterly Journal of the Royal Meteorological*
359 *Society*, 137(656), 553-597, doi: 10.1002/qj.828.

360 Duan, J., Y. Li, F. Wang, and Z. Chen (2019), Multidecadal Change of the Mindanao
361 Current: Is There a Robust Trend?, *Geophysical Research Letters*, 46(12), 6755-
362 6764, doi: 10.1029/2019gl083090.

363 Gergis, J. L., and A. M. Fowler (2009), A history of ENSO events since AD 1525:
364 implications for future climate change, *Climatic Change*, 92(3-4), 343-387, doi:
365 10.1007/s10584-008-9476-z.

366 Xiao-li, G. U., and L. I. Pei-liang (2009), Pacific sea level variations and its factors,
367 *Acta Oceanologica Sinica*, 31(1), 28-36.

368 Hamlington, B. D., S. H. Cheon, P. R. Thompson, M. A. Merrifield, R. S. Nerem, R.
369 R. Leben, and K. Y. Kim (2016), An ongoing shift in Pacific Ocean sea level,
370 *Journal of Geophysical Research-Oceans*, 121(7), 5084-5097, doi:
371 10.1002/2016jc011815.

372 Im, S.-H., S.-I. An, S. T. Kim, and F.-F. Jin (2015), Feedback processes responsible
373 for El Nino-La Nina amplitude asymmetry, *Geophysical Research Letters*,
374 42(13), 5556-5563, doi: 10.1002/2015gl064853.

375 Jin, F. F. (1997), A theory of interdecadal climate variability of the North Pacific
376 ocean-atmosphere system, *Journal of Climate*, 10(8), 1821-1835, doi:
377 10.1175/1520-0442(1997)010<1821:atoicv>2.0.co;2.

378 Jin, F. F., J. S. Kug, S. I. An, and I. S. Kang (2003), A near-annual coupled ocean-
379 atmosphere mode in the equatorial Pacific ocean, *Geophysical Research Letters*,
380 30(2), doi: 10.1029/2002gl015983.

381 Kang, I. S., and J. S. Kug (2002), El Nino and La Nina sea surface temperature
382 anomalies: Asymmetry characteristics associated with their wind stress
383 anomalies, *Journal of Geophysical Research-Atmospheres*, 107(D19), doi:
384 10.1029/2001jd000393.

385 Kang, I. S., and J. S. Kug (2000), An El-Nino prediction system using an intermediate
386 ocean and a statistical atmosphere, *Geophysical Research Letters*, 27(8), 1167-
387 1170, doi: 10.1029/1999gl011023.

388 Kennedy, J. J., N. A. Rayner, R. O. Smith, D. E. Parker, and M. Saunby (2011),
389 Reassessing biases and other uncertainties in sea surface temperature
390 observations measured in situ since 1850: 2. Biases and homogenization, *Journal*
391 *of Geophysical Research-Atmospheres*, 116, doi: 10.1029/2010jd015220.

392 Le Traon, P. Y., F. Nadal, and N. Ducet (1998), An improved mapping method of
393 multisatellite altimeter data, *Journal of Atmospheric and Oceanic Technology*,
394 15(2), 522-534, doi: 10.1175/1520-0426(1998)015<0522:aimmom>2.0.co;2.

395 Li, Y., and W. Han (2015), Decadal Sea Level Variations in the Indian Ocean
396 Investigated with HYCOM: Roles of Climate Modes, Ocean Internal Variability,
397 and Stochastic Wind Forcing, *Journal of Climate*, 28(23), 9143-9165, doi:
398 10.1175/jcli-d-15-0252.1.

399 McCreary, J. (1976), Eastern Tropical Ocean Response to Changing Wind System-

400 with Application to El Nino, *Journal of Physical Oceanography*, 6(5), 632-645,
401 doi: 10.1175/1520-0485(1976)006<0632:etortc>2.0.co;2.

402 Merrifield, M. A. (2011), A Shift in Western Tropical Pacific Sea Level Trends during
403 the 1990s, *Journal of Climate*, 24(15), 4126-4138, doi: 10.1175/2011jcli3932.1.

404 Milne, G. A., W. R. Gehrels, C. W. Hughes, and M. E. Tamisiea (2009), Identifying
405 the causes of sea-level change, *Nature Geoscience*, 2(7), 471-478, doi:
406 10.1038/ngeo544.

407 Nerem, R. S., D. P. Chambers, C. Choe, and G. T. Mitchum (2010), Estimating Mean
408 Sea Level Change from the TOPEX and Jason Altimeter Missions, *Marine*
409 *Geodesy*, 33, 435-446, doi: 10.1080/01490419.2010.491031.

410 Nicholls, R. J., and R. S. J. Tol (2006), Impacts and responses to sea-level rise: A
411 global analysis of the SRES scenarios over the twenty-first century, *Philos.*
412 *Trans. R. Soc. A Math. Phys. Eng. Sci.*, 364(1841), 1073–1095, doi:10.1098/rsta-
413 2006.1754.

414 Nicholls, R. J., P. P. Wong, V. R. Burkett, J. O. Codignotto, J. E. Hay, R. F. McLean,
415 S. Ragoonaden, and C. D. Woodroffe (2007), Coastal systems and low-lying
416 areas, in *Climate Change 2007: Impacts, Adaptation and Vulnerability. Fourth*
417 *Assessment Report of the Intergovernmental Panel on Climate Change (IPCC,*
418 *2007)*, edited by M. L. Parry, O. F. Canziani, J. P. Palutikof, P. J. van der Linden,
419 and C. E. Hanson, Cambridge University Press, Cambridge, UK. pp. 315–356.

420 Nicholls, R. J., and A. Cazenave (2010), Sea-level rise and its impact on coastal zones
421 (June, pg 1517, 2007), *Science*, 329(5992), 628-628.

422 Niedzielski, T., and W. Kosek (2010), El Nino's Impact on the Probability Distribution
423 of Sea Level Anomaly Fields, *Polish Journal of Environmental Studies*, 19(3),
424 611-620.

425 Ohba, M., and H. Ueda (2007), An impact of SST anomalies in the Indian ocean in
426 acceleration of the El Nino to La Nina transition, *Journal of the Meteorological*
427 *Society of Japan*, 85(3), 335-348, doi: 10.2151/jmsj.85.335.

428 Okumura, Y. M., and C. Deser (2010), Asymmetry in the Duration of El Nino and La
429 Nina, *Journal of Climate*, 23(21), 5826-5843, doi: 10.1175/2010jcli3592.1.

430 Qiu, B., and S. Chen (2010), Interannual-to-Decadal Variability in the Bifurcation of
431 the North Equatorial Current off the Philippines, *Journal of Physical*
432 *Oceanography*, 40(11), 2525-2538, doi: 10.1175/2010jpo4462.1.

433 Qiu, B., and S. Chen (2012), Multidecadal Sea Level and Gyre Circulation Variability
434 in the Northwestern Tropical Pacific Ocean, *Journal of Physical Oceanography*,
435 42(1), 193-206, doi: 10.1175/jpo-d-11-061.1.

436 Qiu, B., S. Chen, and H. Sasaki (2013), Generation of the North Equatorial
437 Undercurrent Jets by Triad Baroclinic Rossby Wave Interactions, *Journal of*
438 *Physical Oceanography*, 43(12), 2682-2698, doi: 10.1175/jpo-d-13-099.1.

439 Qiu, B., S. Chen, L. Wu, and S. Kida (2015), Wind- versus Eddy-Forced Regional Sea
440 Level Trends and Variability in the North Pacific Ocean, *Journal of Climate*,
441 28(4), 1561-1577, doi: 10.1175/jcli-d-14-00479.1.

442 Ren, Q., Y. Li, F. Wang, J. Duan, S. Hu, and F. Wang (2020), Variability of the
443 Mindanao Current Induced by El Niño Events, *Journal of Physical*

444 Oceanography, 0(0), null, doi: 10.1175/jpo-d-19-0150.1.

445 Palanisamy, H., A. Cazenave, T. Delcroix, and B. Meyssignac (2015), Spatial trend
446 patterns in the Pacific Ocean sea level during the altimetry era: the contribution
447 of thermocline depth change and internal climate variability, *Ocean Dynamics*,
448 65(3), 341-356, doi: 10.1007/s10236-014-0805-7.

449 Stammer, D., A. Cazenave, R. M. Ponte, and M. E. Tamisiea (2013), Causes for
450 Contemporary Regional Sea Level Changes, in *Annual Review of Marine*
451 *Science*, Vol 5, edited by C. A. Carlson and S. J. Giovannoni, pp. 21-46.

452 Su, J., R. Zhang, T. Li, X. Rong, J. S. Kug, and C.-C. Hong (2010), Causes of the El
453 Nino and La Nina Amplitude Asymmetry in the Equatorial Eastern Pacific,
454 *Journal of Climate*, 23(3), 605-617, doi: 10.1175/2009jcli2894.1.

455 Sverdrup, H. U. (1947), NOTE ON THE CORRECTION OF REVERSING
456 THERMOMETERS, *Journal of Marine Research*, 6(2), 136-138.

457 Swerczynska, M., T. Niedzielski, and W. Kosek (2014), Semiannual and annual
458 oscillations of sea level and their impact on asymmetry between El Nino and La
459 Nina episodes, *Studia Geophysica Et Geodaetica*, 58(2), 302-325, doi:
460 10.1007/s11200-013-1124-z.

461 White, G. H. (1980), SKEWNESS, KURTOSIS AND EXTREME VALUES OF
462 NORTHERN HEMISPHERE GEOPOTENTIAL HEIGHTS, *Monthly Weather*
463 *Review*, 108(9), 1446-1455, doi: 10.1175/1520-
464 0493(1980)108<1446:skaevo>2.0.co;2.

465 Wyrtki, K. (1975), EL NINO - DYNAMIC-RESPONSE OF EQUATORIAL PACIFIC

466 OCEAN TO ATMOSPHERIC FORCING, *Journal of Physical Oceanography*,
467 5(4), 572-584, doi: 10.1175/1520-0485(1975)005<0572:entdro>2.0.co;2.

468 Zebiak, S. E. (1989), OCEANIC HEAT-CONTENT VARIABILITY AND EL NINO
469 CYCLES, *Journal of Physical Oceanography*, 19(4), 475-486, doi:
470 10.1175/1520-0485(1989)019<0475:ohcvae>2.0.co;2.

471 Zhang, X., and J. A. Church (2012), Sea level trends, interannual and decadal
472 variability in the Pacific Ocean, *Geophysical Research Letters*, 39(21), doi:
473 10.1029/2012gl053240.
474

475 **Figure captions**

476 **Figure 1.** Standard deviation (STD) of sea level anomalies (SLAs, m) of 1993-2016
477 from (a) AVISO sea level product and (b) HYCOM-CTL. (c) Skewness of SLAs. (d)
478 Regression coefficient $k_{\text{Niño}}$ (m) of SLAs onto the normalized Niño-3.4 index for El
479 Niño condition (Niño-3.4 > 0). (e) Same as (b) but for La Niña condition (Niño-3.4 <
480 0). (f) Ratio of $k_{\text{Niño}}$ to $k_{\text{Niña}}$, i.e., $R_k = k_{\text{Niño}}/k_{\text{Niña}}$. SLA data in (c)-(f) are derived from
481 AVISO sea level product of 1993-2016.

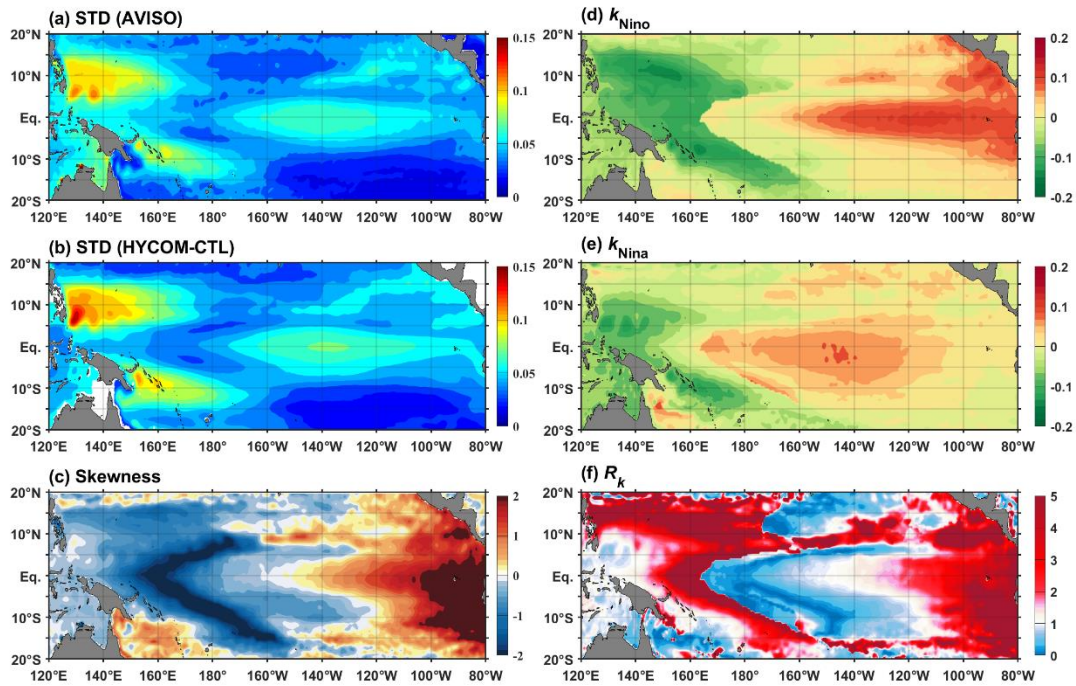
482 **Figure 2.** R_k distributions during 1993-2016 simulated by (a) HYCOM-CTL, (b)
483 HYCOM-TAU, and (c) RGO-CTL. (d)-(f) are the same as (a)-(c), but for the 1979-
484 2016 period.

485 **Figure 3.** R_k distributions from (a) EXP1, (b) EXP2, (c) EXP1-TAUX and (d) EXP2-
486 TAUX. (e) and (f) show the 1st singular value decomposition (SVD) modes for zonal
487 wind stress τ^x (N m^{-2} ; solid and dashed contours for positive and negative values)
488 and upper-layer thickness ULT (m; color shading) of EXP1-TAUX1 for El Niño and
489 La Niña conditions, respectively.

490 **Figure 4.** (a) Zonal structure of the 5°S-5°N average τ^x (left), and ULT (middle) of
491 the 1st SVD mode, and regression coefficients ($k_{\text{Niño}}$ and $k_{\text{Niña}}$; right) in EXP1-TAUX,
492 computed separated for the for El Niño and La Niña conditions. (b) Same as (a) but
493 for EXP2-TAUX. (c) is the same as (a), but for τ^x of the 1st SVD mode in RGO-
494 CTL, and theoretically-predicted ULT and regression coefficients (see the text for
495 details), and they are normalized by the standard deviation.

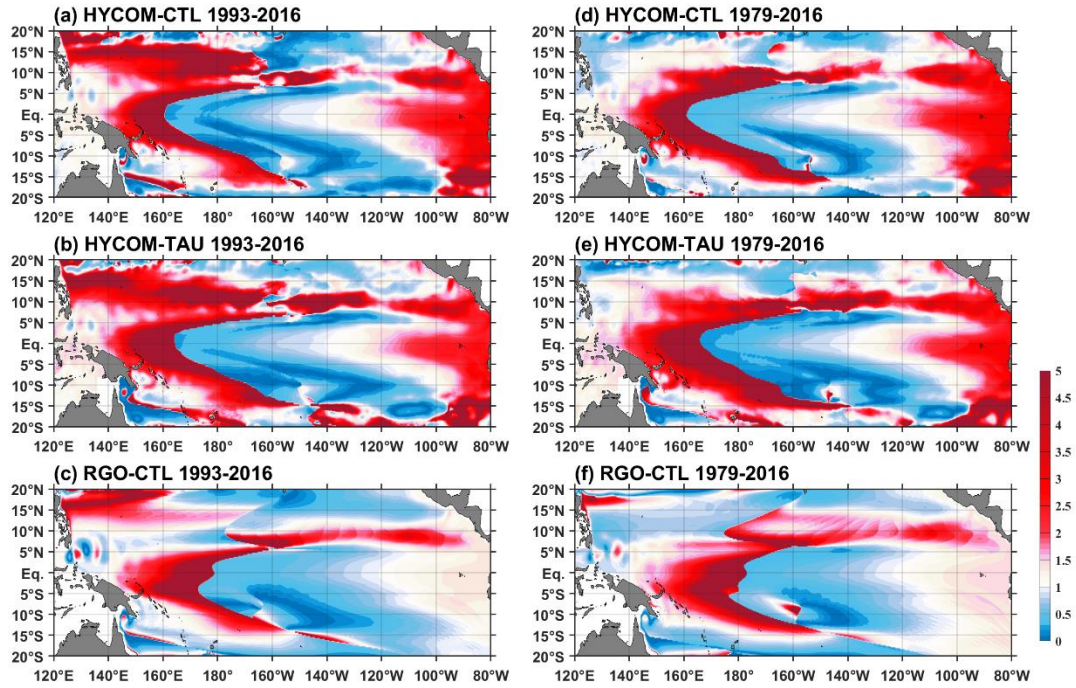
496

497 **Figures**



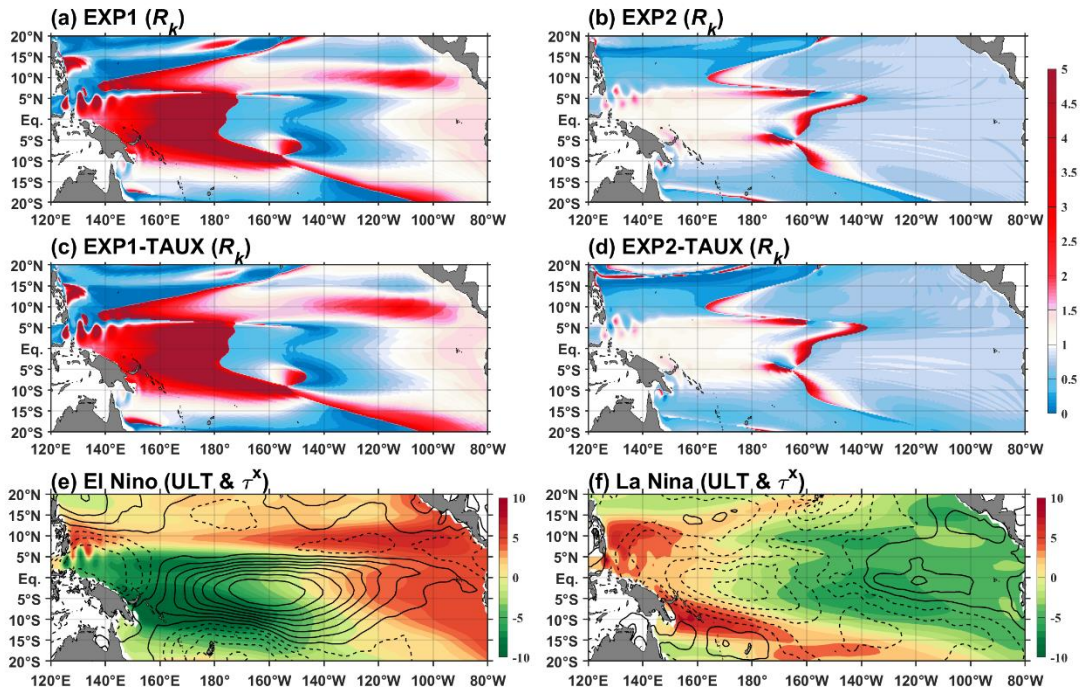
498

499 **Figure 1.** Standard deviation (STD) of sea level anomalies (SLAs, m) of 1993-2016
500 from (a) AVISO sea level product and (b) HYCOM-CTL. (c) Skewness of SLAs. (d)
501 Regression coefficient k_{Nino} (m) of SLAs onto the normalized Niño-3.4 index for El
502 Niño condition (Niño-3.4 > 0). (e) Same as (b) but for La Niña condition (Niño-3.4 <
503 0). (f) Ratio of k_{Nino} to k_{Nina} , i.e., $R_k = k_{Nino}/k_{Nina}$. SLA data in (c)-(f) are derived from
504 AVISO sea level product of 1993-2016.



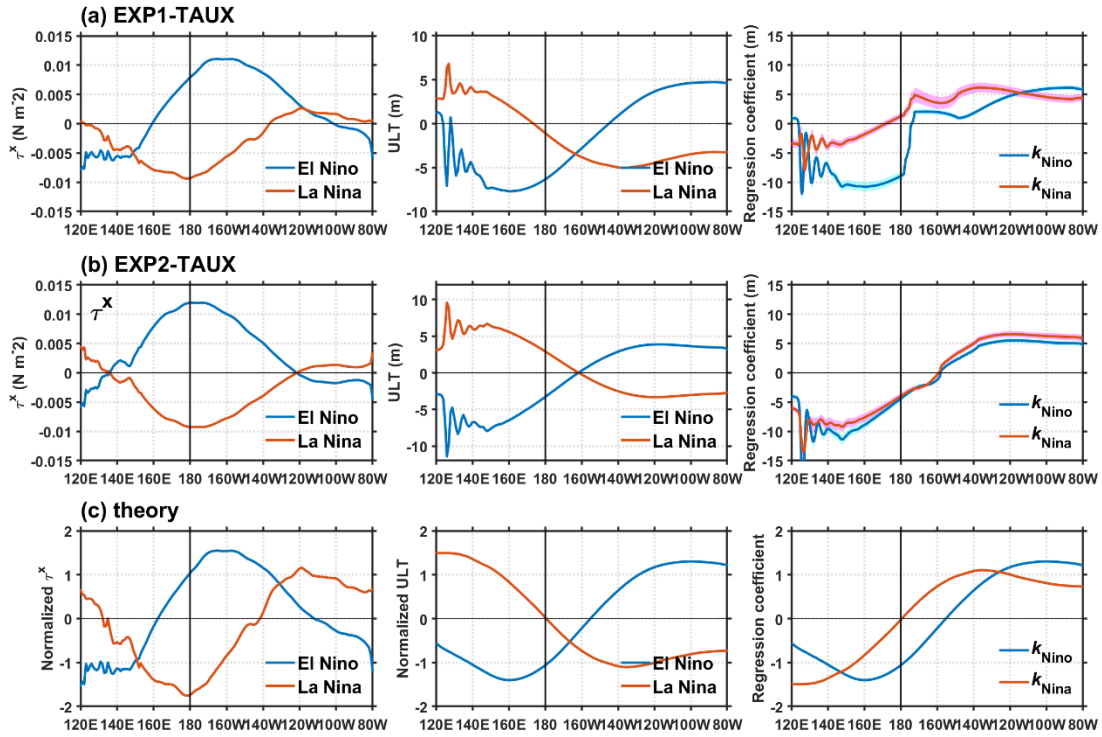
505

506 **Figure 2.** R_k distributions during 1993-2016 simulated by (a) HYCOM-CTL, (b)
 507 HYCOM-TAU, and (c) RGO-CTL. (d)-(f) are the same as (a)-(c), but for the 1979-
 508 2016 period.



509

510 **Figure. 3.** R_k distributions from (a) EXP1, (b) EXP2, (c) EXP1-TAUX and (d) EXP2-
 511 TAUX. (e) and (f) show the 1st singular value decomposition (SVD) modes for zonal
 512 wind stress τ^x (N m⁻²; solid and dashed contours for positive and negative values) and
 513 upper-layer thickness ULT (m; color shading) of EXP1-TAUX1 for El Niño and La
 514 Niña conditions, respectively.



515

516 **Figure. 4.** (a) Zonal structure of the 5°S-5°N average τ^x (left), and ULT (middle) of
 517 the 1st SVD mode, and regression coefficients (k_{Nino} and k_{Nina} ; right) in EXP1-TAUX,
 518 computed separated for the for El Niño and La Niña conditions. (b) Same as (a) but
 519 for EXP2-TAUX. (c) is the same as (a), but for τ^x of the 1st SVD mode in RGO-
 520 CTL, and theoretically-predicted ULT and regression coefficients (see the text for
 521 details), and they are normalized by the standard deviation.

Asymmetric Responses of the Western tropical Pacific
Sea level to El Niño and La Niña

Qiuping Ren^{1,2}, Yuanlong Li^{1,3,4}, Fei Zheng^{3,5}, Fan

Wang^{1,2,3,4}, Jing Duan^{1,3,4}

¹Key Laboratory of Ocean Circulation and Waves, Institute of Oceanology, Chinese Academy of Sciences, Qingdao, China, ²University of Chinese Academy of Sciences, Beijing, China, ³Center for Ocean Mega-Science, Chinese Academy of Sciences, Qingdao, China, ⁴Function Laboratory for Ocean Dynamics and Climate, Qingdao National Laboratory for Marine Science and Technology, Qingdao, China, ⁵International Center for Climate and Environment Science, Institute of Atmospheric Physics, Chinese Academy of Sciences, Beijing, China,

Contents of this file

Figure S1

Figure S2

Figure S3

Figure S4

Table S1

Figure S5

Figure S6

Figure S7

Introduction

Seven figures and one table are uploaded as supporting information. **Figure S1** shows composites of sea level anomalies (SLAs) from AVISO for the mature phases of El Niño and La Niña conditions. **Figure S2** shows the lead-lag months of SLAs and Niño-3.4 index and Ratio of the synchronous-regressed coefficients $k_{\text{Niño}}$ and $k_{\text{Niña}}$. **Figure 3** shows the time series of the normalized SLAs at three tidal gauge station from different datasets. **Figure S4** shows the distributions of the 1st SVD mode for the sea surface temperature and wind stress of different condition during 1979-2016. **Table S1** shows the model experiments descriptions of HYCOM and 1.5-layer RGO. **Figure S5** shows the time-longitude plots of normalized ULT anomaly from RGO-CTL, EXP1, and SVD2. **Figure S6** shows R_k produced by SVD2, SVDD5, and SVD10. **Figure S7** shows R_k produced by EXP3.

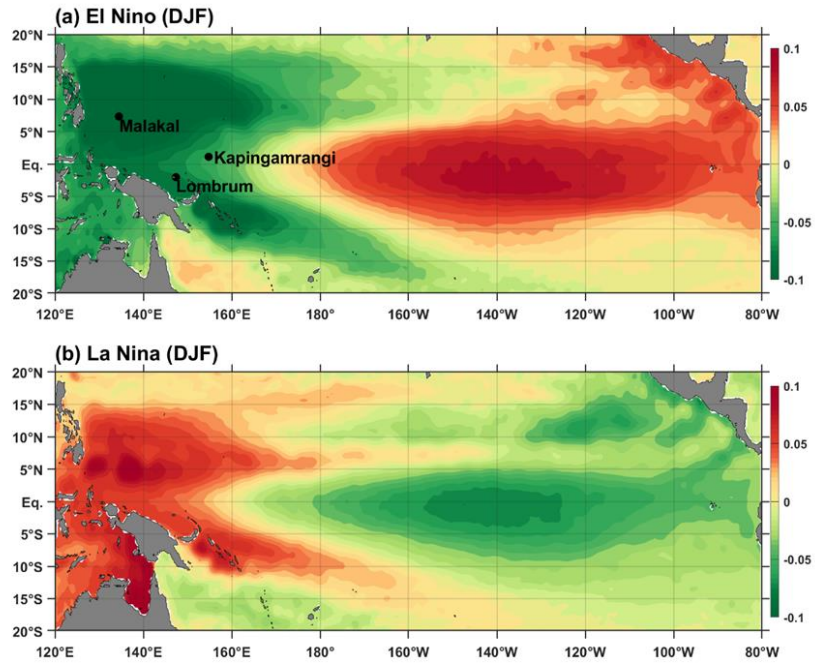


Figure S1. Composites of sea level anomalies (SLAs, m) from AVISO for the mature phases (December, January, and February, DJF) of (a) El Niño and (b) La Niña conditions during 1993-2016. The black dots at (7.33°N, 134.47°E), (1.1°N, 154.78°E) and (2.04°S, 147.47°E) indicate the Malakal, Kapingamrangi, and Lombrum tidal gauge stations.

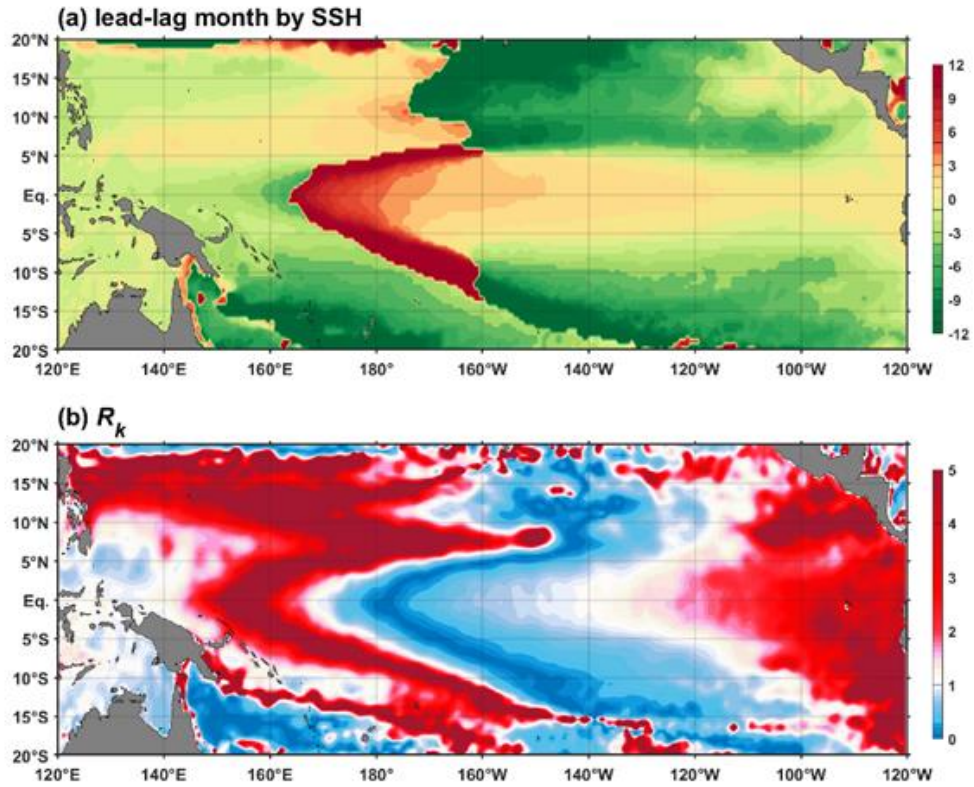


Figure S2. (a) The lead-lag months of SLAs and Niño-3.4 index. (b) Ratio of k_{Nino} to k_{Nina} , i.e., $R_k = k_{\text{Nino}}/k_{\text{Nina}}$. k_{Nino} and k_{Nina} are the synchronous regression coefficients of SLAs during El Niño (Niño-3.4 > 0) and La Niña (Niño-3.4 < 0) condition onto the normalized Niño-3.4 index, respectively. SLA data are derived from AVISO sea level product of 1993-2016.

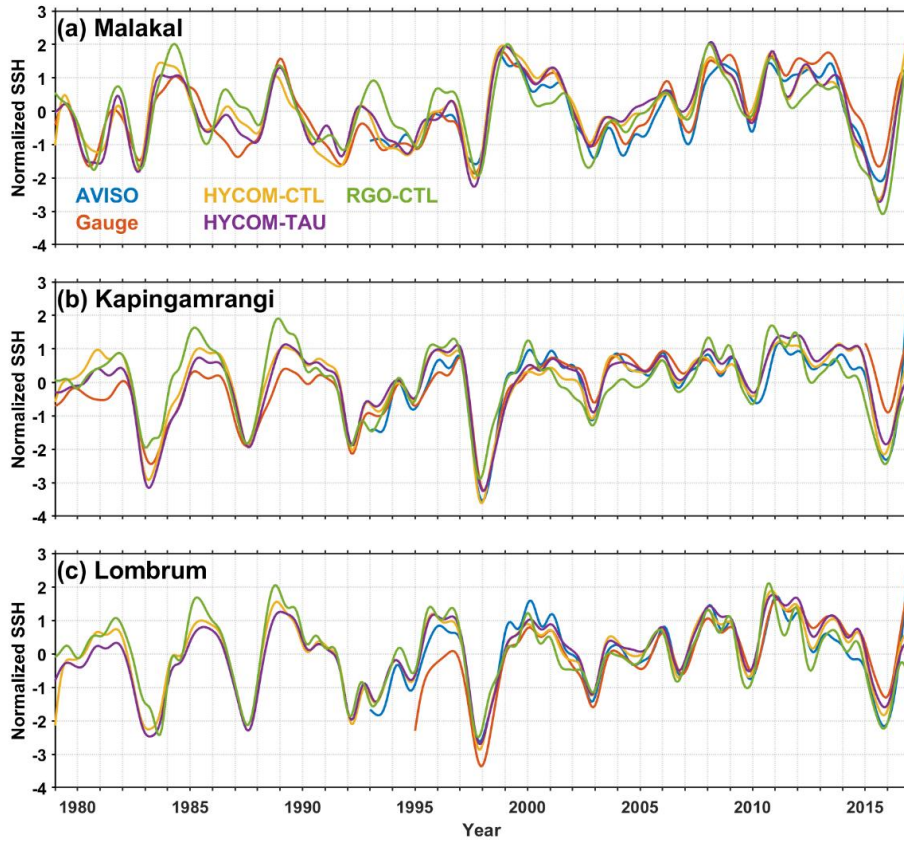


Figure S3. Time series of the normalized SLAs at (a) Malakal, (b) Kapingamrangi, (c) Lombrum from AVISO, tidal gauge, HYCOM-CTL, HYCOM-TAU and RGO-CTL. All the time series are 13-month low-passed filtered and normalized by the standard deviation. The normalized upper-layer thickness (ULT) anomaly in RGO-CTL represents SSH anomalies to compare with other datasets.

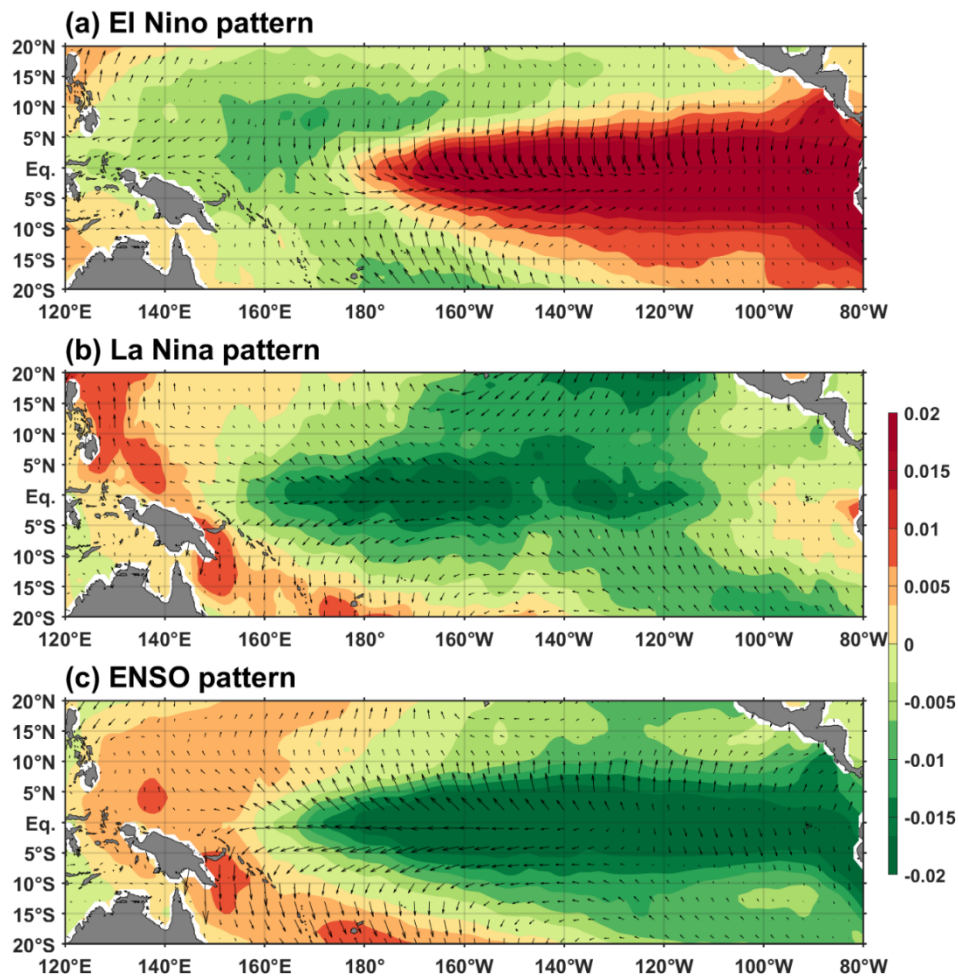


Figure S4. (a) Distributions of the 1st SVD mode for the sea surface temperature (SST; color shading) and wind stress (vector) of El Niño condition during 1979-2016. (b) and (c) are the same as (a), but for La Niña condition and ENSO condition, respectively. ENSO condition does not distinguish El Niño and La Niña conditions.

Table S1. HYbrid Coordinate Ocean Model (HYCOM) and 1.5-layer nonlinear reduced gravity ocean (RGO) Model experiments descriptions.

Exp. Name	Forcing
HYCOM-CTL	Daily ERA-Interim atmospheric fields
HYCOM-TAU	Daily ERA-Interim wind stress, but all the other forcing fields are fixed to monthly climatology
RGO-CTL	Monthly ERA-interim wind stress
EXP1	Reconstructed wind stress for El Niño and La Niña phase based on the 1 st SVD mode of SST and wind stress
EXP2	Reconstructed wind stress for all the period based on the 1 st SVD mode of SST and wind stress
EXP1-TAUX	Same as EXP1, but the meridional wind stress τ^y is fixed to monthly climatology
EXP2-TAUX	Same as EXP2, but the meridional wind stress τ^y is fixed to monthly climatology
EXP3	Reconstructed wind stress , $\tau(x, y, t) = V_{\tau}(x, y)T(t)$ x, y and t indicate the zonal, meridional and time grid points, respectively. V_{τ} is the 1 st SVD singular vectors for wind stress. $T(t)$ is the idealized Niño-3.4 index and is a time-varying sinusoidal function with a timescale of 4 years, $\sin(t/4)$. EXP3 makes use of the 1 st mode only and is integrated for 50 years.
SVD2	Same as EXP1, but reconstructed wind stress based on the first two SVD modes
SVD5	Same as EXP1, but reconstructed wind stress based on the first five SVD modes
SVD10	Same as EXP1, but reconstructed wind stress based on the first ten SVD modes

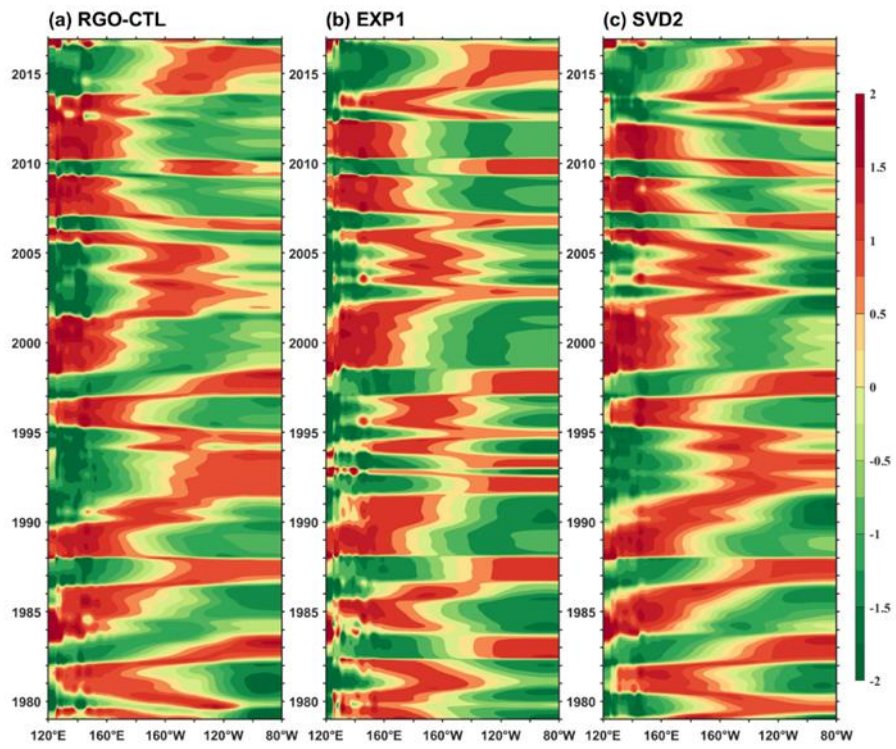


Figure S5. Time-longitude plots of normalized ULT anomaly from (a) RGO-CTL, (b) EXP1, and (c) SVD2.

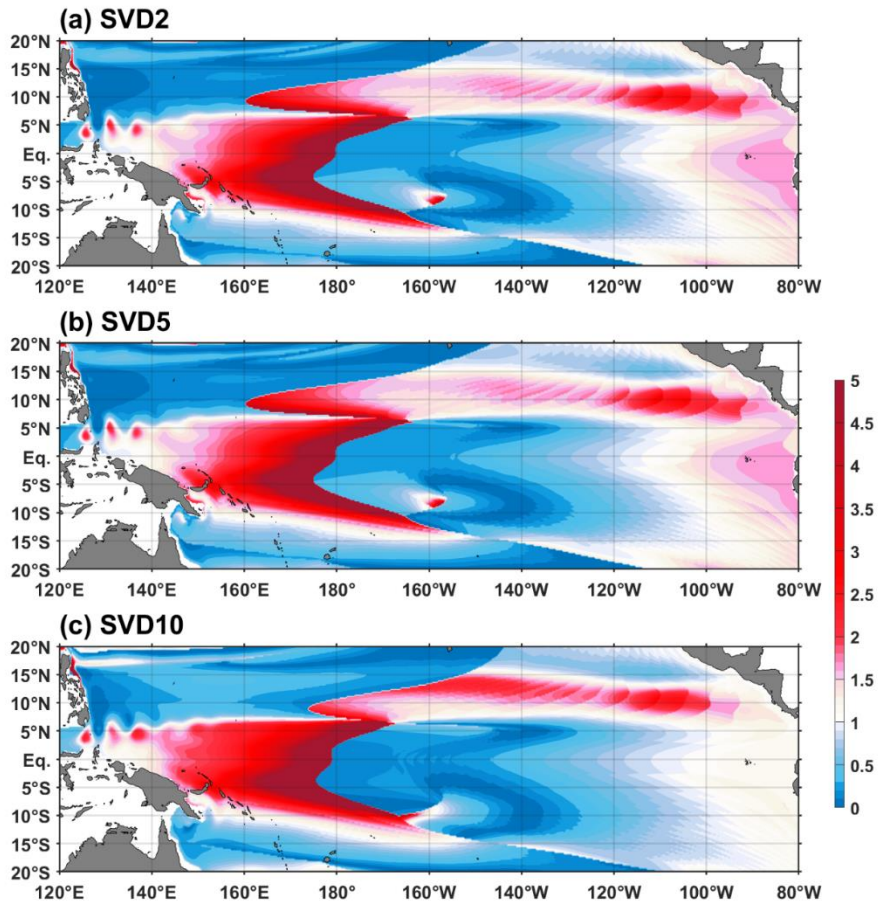


Figure S6. R_k produced by (a) SVD2, (b) SVD5, and (c) SVD10. k_{Nino} and k_{Nina} are the regression coefficients of ULT anomaly during El Niño (Niño-3.4 > 0) and La Niña (Niño-3.4 < 0) condition onto the normalized Niño-3.4 index, respectively.

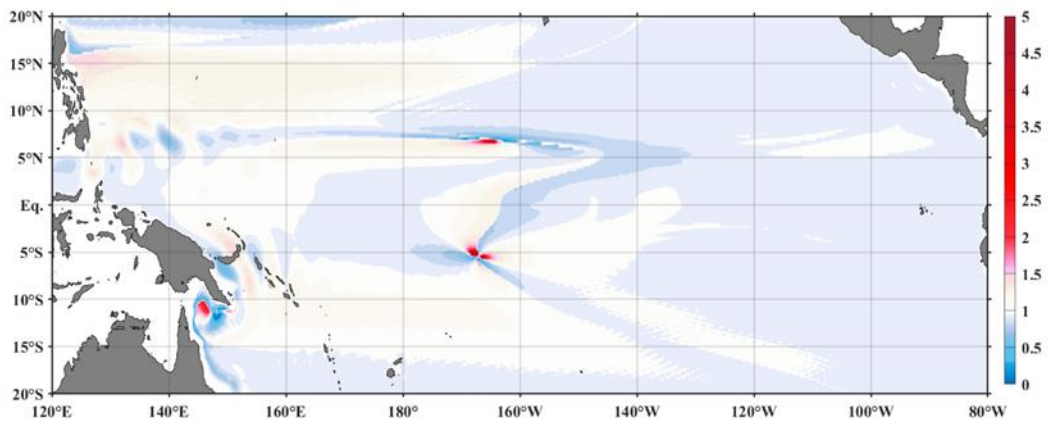


Figure S7. R_k produced by EXP3.